MIT OpenCourseWare
http://ocw.mit.edu

Continuum Electromechanics

For any use or distribution of this textbook, please cite as follows:

Melcher, James R. *Continuum Electromechanics*. Cambridge, MA: MIT Press, 1981.
Copyright Massachusetts Institute of Technology. ISBN: 9780262131650. Also
available online from MIT OpenCourseWare at http://ocw.mit.edu (accessed MM DD,
YYYY) under Creative Commons license Attribution-NonCommercial-Share Alike.

For more information about citing these materials or our Terms of Use, visit:
http://ocw.mit.edu/terms.

6

Magnetic Diffusion and Induction
Interactions

6.1 Introduction

Except that magnetoquasistatic rather than electroquasistatic systems are considered, in this chapter electromechanical phenomena are studied from the same viewpoint as in Chap. 5. Material deformations are again prescribed (kinematic) while the magnetic field sources, the distributions of current or magnetization density, evolve in a dynamical manner that is self-consistently described throughout the volume of interest. Most of the discussion in this chapter relates to magnetic diffusion with material convection.

In practical terms, this chapter takes leave of the windings and associated slip rings or commutators used in Chap. 4 to constrain current distributions in moving elements and takes up conductors in which the currents seek a distribution consistent with the magnetoquasistatic field laws and the imposed motion. The magnetic induction machine is an important example. Most often encountered as a rotating machine, it might also have as a moving member a "linear" sheet of metal or even a liquid. The study of temporal and spatial transients and of boundary layer models in Secs. 6.9-6.11 is pertinent to the linear induction machines, whether they be applied to train propulsion or manufacture of sheet metal. The "deep conductor" interactions considered in Secs. 6.6 and 6.7 give insights concerning liquid-metal induction pumping, a topic continued in Chap. 9.

The boundary conditions and transfer relations summarized in Secs. 6.3 and 6.5 are a basic resource for developing analytical models representing systems suggested by the case studies of Secs. 6.4 and 6.6. Similarly, the dissipation and skin-effect relations developed in Secs. 6.7 and 6.8 are designed to be of general applicability.

Much of the magnetic diffusion phenomena developed in this chapter, the mathematical relations as well as the physical insights, pertain as well to the diffusion of molecules or of heat. Hence, dividends from an investment in this chapter are in part collectable in Chap. 9. In addition, what in Sec. 6.2 is a theorem concerning the conservation of flux for material surfaces of fixed identity, in Chaps. 7 and 9 relates to fluid mechanics and becomes Kelvin's vorticity theorem. Diffusion of vorticity, a momentum transfer process in fluids taken up in Chap. 7, has much in common with magnetic diffusion.

The conduction model in this chapter is exclusively ohmic. The model is especially appropriate in the relatively highly conducting materials of interest if magnetic diffusion effects are an issue. Typically, conductors are solid or liquid metals, or perhaps highly ionized gases. The development is purposely one that parallels the sections on ohmic conductors in electroquasistatic systems, Secs. 5.10-5.16. A comparative study of electroquasistatic and magnetoquasistatic rate processes, models and examples results in the recognition of both analogies and contrasts.

Although resistive types of induction interactions are by far the most common, time-average forces can be developed through phase shifts created by other types of loss mechanisms. The important example of magnetization hysteresis interactions is used in Sec. 6.12 to exemplify not only how time-average magnetization forces can be developed, but by analogy, how polarization interactions can be created in an electroquasistatic context.

6.2 Magnetic Diffusion in Moving Media

For a material at rest in the primed frame of reference, Ohm's law is

$$\vec{J}_f' = \sigma \vec{E}'$$ (1)

where the conductivity σ is in general a function of position and time. This law, introduced in Sec. 3.3, implies at least two charge-carrier species and a Hall parameter (Eq. 3.3.4) that is small compared to unity. Use of the field transformations $\vec{J}_f = \vec{J}_f'$ (Eq. 2.5.11b) and $\vec{E}' = \vec{E} + \vec{v} \times \mu_0 \vec{H}$ (Eq. 2.5.12b) expresses Eq. 1 in the laboratory frame of reference,

$$\vec{J}_f = \sigma(\vec{E} + \vec{v} \times \mu_0 \vec{H})$$ (2)

where $\vec{v}$ is the velocity of the material having the conductivity σ. This generalization of Ohm's law to represent conduction in a moving material is clearly valid provided that the material is moving with a constant velocity. But the law will be used throughout this chapter for materials that are accelerating. The assumption is made that accelerations have a negligible effect on the processes responsible for the conduction, for example, in a metallic conductor, that the acceleration of the ponderable material has a negligible effect on electronic motions.

Solution of Eq. 2 for $\vec{E}$ gives an expression that can be substituted into Faraday's law, Eq. 2.3.25b, to obtain

$$\nabla \times \left(\frac{\vec{J}_f}{\sigma}\right) = -\frac{\partial \vec{B}}{\partial t} + \nabla \times (\vec{v} \times \vec{B}) \tag{3}$$

where the definition $\vec{B} \equiv \mu_o(\vec{H} + \vec{M})$ has been used.

The embodiment of Ohm's and Faraday's laws, represented by Eq. 3, has a simple physical significance best seen by considering the integral form of these same laws. With $\vec{E}'$ replaced using Eq. 1, Faraday's integral law, Eq. 2.7.3b, becomes

$$\oint_C \frac{\vec{J}_f}{\sigma} \cdot d\vec{\ell} = -\frac{d}{dt} \int_S \vec{B} \cdot \vec{n} da \tag{4}$$
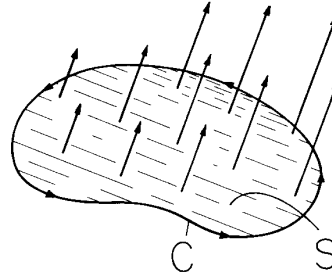

Fig. 6.2.1

Surface of fixed identity.

In writing this equation, the surface S enclosed by the contour C, Fig. 6.2.1, is one of fixed identity (one attached to the deforming material), so $\vec{v} = \vec{v}_s$. (The same expression would be obtained by integrating Eq. 3 over a surface of fixed identity and applying the generalized Leibnitz rule, Eq. 2.6.4.)

According to Eq. 4, the dissipation of total flux linked by a surface of fixed identity is proportional to the "iR" drop around the contour of fixed identity enclosing the surface. The statement is a generalization of one representing an ideal deforming inductor having the terminal variables (λ, i) shorted by a resistance R:
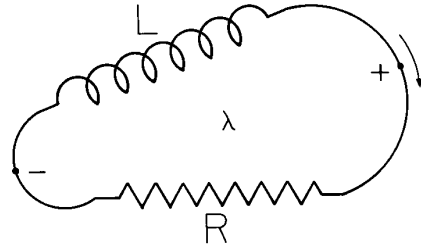
$$iR = -\frac{d\lambda}{dt} \tag{5}$$

Fig. 6.2.2

Circuit equivalent to C in Fig. 6.2.1.

In the limit of "infinite" conductivity, the flux intercepted by a surface of fixed identity is invariant Equations 3 and 4 represent the same laws, so if the left side of Eq. 3 is negligible, it too implies that the flux linking a contour of fixed identity is conserved. The circuit helps to emphasize that in most of the chapter the subject is distributed "resistors" and "inductors" typified in their dynamics by "L/R" time constants.

Ampère's law, Eq. 2.3.23b, eliminates $\vec{J}_f$ from Eq. 3 in favor of $\vec{H}$. With magnetization described $\vec{B} = \mu\vec{H}$, where μ can be a function of space and time but not of $\vec{H}$, Eq. 3 then becomes

$$\nabla \times \frac{1}{\sigma}(\nabla \times \frac{1}{\mu}\vec{B}) = -\frac{\partial \vec{B}}{\partial t} + \nabla \times (\vec{v} \times \vec{B}) \tag{6}$$

In regions where the properties (σ, μ) and material velocity $\vec{v}$ are uniform, Eq. 6 becomes the convective diffusion equation*

$$\frac{1}{\mu\sigma} \nabla^2 \vec{B} = (\frac{\partial}{\partial t} + \vec{v} \cdot \nabla)\vec{B} \tag{7}$$

On the right is the rate of change with respect to time for an observer moving with the velocity $\vec{v}$ of the material (Sec. 2.4). This convective derivative represents two ways in which time rates of change are experienced by a given element of material. Perhaps created by a time-varying field source, at a given fixed location there is a magnetic induction $\partial \vec{B}/\partial t$ with a rate characterized by a time τ. Motion of the material through a spatially varying field gives rise to a second magnetic induction contribution generally represented by the "speed" term $\nabla \times (\vec{v} \times \vec{B})$ (Eq. 6) and particularly reduced to $\vec{v} \cdot \nabla\vec{B}$ in Eq. 7. This contribution is characterized by a transport time ℓ/u, where ℓ and u are respectively a typical length and velocity. Parameters representing the competition between these two rates of change and the diffusion process are identified by writing Eq. 7 in terms of the dimensionless variables

$$t = \underline{t}\tau; \quad \vec{v} = \underline{\vec{v}}u; \quad (x,y,z) = (\underline{x},\underline{y},\underline{z})\ell \tag{8}$$

---

*$\nabla \times (\vec{v} \times \vec{B}) \equiv \vec{v}(\nabla \cdot \vec{B}) - \vec{B}(\nabla \cdot \vec{v}) + \vec{B} \cdot \nabla\vec{v} - \vec{v} \cdot \nabla\vec{B}; \quad \nabla \cdot \vec{v} = 0, \nabla \cdot \vec{B} = 0, \nabla\vec{v} = 0$
$\nabla \times (\nabla \times \vec{B}) \equiv \nabla(\nabla \cdot \vec{B}) - \nabla^2\vec{B}$

Note that either Eq. 6 or Eq. 7 is linear in $\vec{B}$, so that the flux density need not be normalized. In terms of these variables, Eq. 7 becomes

$$\nabla^2 \vec{B} = \frac{\tau_m}{\tau} \frac{\partial \vec{B}}{\partial t} + R_m \vec{v} \cdot \nabla \vec{B} \tag{9}$$

where

$\tau_m = \mu \sigma \ell^2$: magnetic diffusion time

$R_m = \mu \sigma u \ell$: magnetic Reynolds number

For μ, σ and $\vec{v}$ not uniform, τ_m and R_m are defined using typical magnitudes of these quantities.

If the diffusion term on the left in Eq. 9 (in Eq. 4) is negligible, the dynamics tend to be flux conserving. Thus, τ_m/τ and R_m are dimensionless numbers, really representing the same physical process, that are an index to the degree of flux conservation. If a process is steady so that $\partial \vec{B}/\partial t = 0$, then R_m, which is the ratio of the magnetic diffusion time to a typical transport time ℓ/u, is the appropriate index. If R_m is large, material convection tends to dominate in determining the field distribution.

Few physical situations involve only one dimension. Usually, practical systems are heterogeneous, in that they are made up of materials having different electrical properties each with its own dimensions. As a result, a model may involve several different τ_m's and R_m's. Identifying the most critical diffusion times and magnetic Reynolds numbers is an art developed by having as background examples such as those in the following sections.

Skin effect, a magnetic diffusion phenomenon, is conventionally characterized by the skin depth δ_m. As a parameter representing the extent to which a sinusoidal steady-state magnetic field diffuses into a conductor, it embodies the magnetic diffusion time τ_m. The extent to which the field diffuses into an "infinite" conductor is itself the characteristic length ℓ, while the characteristic time is the reciprocal of the imposed field frequency. In fact, setting $\tau_m/\tau = \mu \sigma \delta^2 \omega = 2$ results in what will be identified in Sec. 6.6 as the magnetic skin depth:

$$\delta = \sqrt{\frac{2}{\omega \mu \sigma}} \tag{10}$$

The skin depth is the length that makes the magnetic diffusion time equal to twice the reciprocal angular frequency of a sinusoidal driving field.

Typical electrical conductivities for materials in which magnetic diffusion is of interest are given in Table 6.2.1. For these materials, the magnetic diffusion time, τ_m, is given as a function of the characteristic length ℓ in Fig. 6.2.3 and the skin depth, δ, is given as a function of frequency $f = \omega/2\pi$ in Fig. 6.2.4.

Table 6.2.1. Typical electrical conductivities of materials in which magnetic diffusion is of interest. Permeability is essentially μ_0 unless otherwise stated.

| Material	Conductivity σ (mhos/m)
Solids	
Copper	5.80×10^7
4% silicon-iron	1.7×10^6 ($\mu \sim 5000 \ \mu_0$)
Silver	6.17×10^7
Aluminum	3.72×10^7
Graphite	7.27×10^4
Liquids	
Mercury	1.06×10^6
Sodium	1.04×10^7
Sodium potassium 22%-78%	2.66×10^6
Cerrelow-117 (tin-bismuth-lead-antimony alloy)	1.9×10^6
Seawater	4
Deionized pure water	4×10^{-6}
Alumium	4.31×10^6 (870°C)
Tin	2.1×10^6 (231.9°C)
Zinc	2.83×10^6 (419°C)
Gases	
Typical seeded combustion gases	~ 40
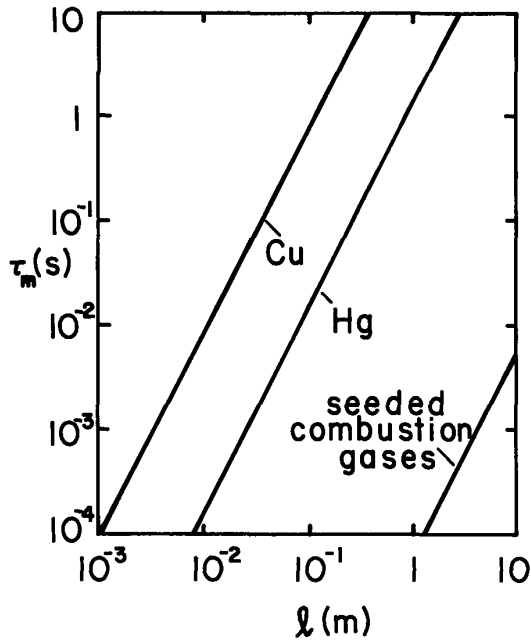
Fig. 6.2.3. Magnetic diffusion time as a function
of characteristic length for solid copper,
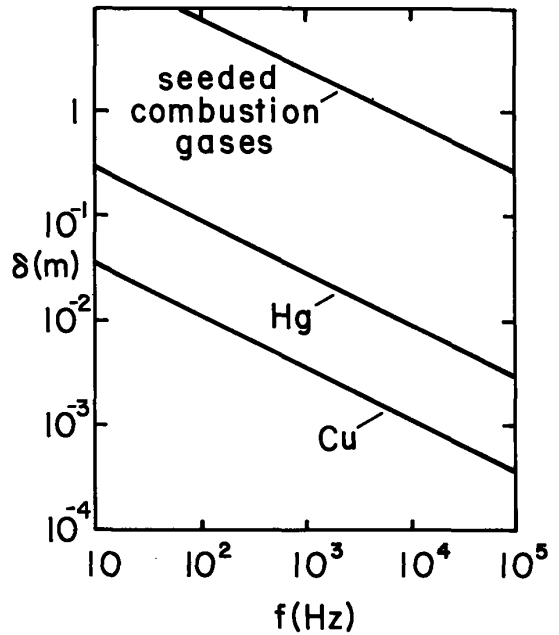liquid mercury and gas typical of that used
in MHD generator.

Fig. 6.2.4. Skin depth as function
of frequency for materials of
Fig. 6.2.3.

6.3 Boundary Conditions for Thin Sheets and Shells

Currents induced in a sufficiently thin conductor
can be regarded as essentially uniform over its cross
section. Some of the most important models for magnetic
diffusion exploit the resulting simplification of the
field representation. The magnetic diffusion process is
condensed into a boundary condition at the surface
occupied by the conductor, in Fig. 6.3.1, the surface
separating regions (a) and (b).

Because the conducting sheet is bounded from either
side by insulators, the current distribution is essen-
tially that of a surface current

Fig. 6.3.1. Conducting sheet having normal
flux density B_n, thickness Δ and hence
surface conductivity $\sigma_s = \Delta\sigma$.

$$\vec{K}_f = \Delta\sigma\vec{E}_t \equiv \sigma_s\vec{E}_t \tag{1}$$

The normal flux density is continuous, so it is denoted by B_n without distinguishing between regions (a)
and (b).

Ohm s law and Faraday's law are embodied in Eq. 6.2.3. For the present purposes, the normal com-
ponent of this equation is the essential one. Multiplied by the sheet thickness, Δ, it becomes

$$(\nabla \times \vec{K}_f)_n = -\sigma_s \frac{\partial B_n}{\partial t} + \sigma_s[\nabla \times (\vec{v} \times \vec{B})]_n \tag{2}$$

Continuity of current (Eq. 2.3.26) requires that

$$\nabla_\Sigma \cdot \vec{K}_f = 0 \tag{3}$$

where $\nabla_\Sigma \cdot$ is the two-dimensional divergence, the usual divergence with the vector component normal to
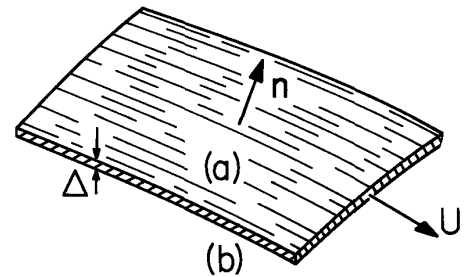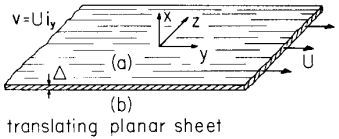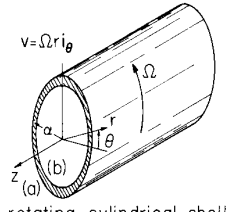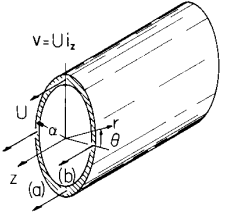the surface omitted.

Configuration	Boundary condition
translating planar sheet	$\left(\dfrac{\partial^2}{\partial y^2} + \dfrac{\partial^2}{\partial z^2}\right) [\![H_y]\!] = -\sigma_s \dfrac{\partial}{\partial y} \left(\dfrac{\partial}{\partial t} + U \dfrac{\partial}{\partial y}\right) B_x$ (a)
rotating cylindrical shell	$\left(\dfrac{1}{\alpha^2} \dfrac{\partial^2}{\partial \theta^2} + \dfrac{\partial^2}{\partial z^2}\right) [\![H_\theta]\!] = -\dfrac{\sigma_s}{\alpha} \dfrac{\partial}{\partial \theta} \left(\dfrac{\partial}{\partial t} + \Omega \dfrac{\partial}{\partial \theta}\right) B_r$ (b)
translating cylindrical shell	$\left(\dfrac{1}{\alpha^2} \dfrac{\partial^2}{\partial \theta^2} + \dfrac{\partial^2}{\partial z^2}\right) [\![H_z]\!] = -\sigma_s \dfrac{\partial}{\partial z} \left(\dfrac{\partial}{\partial t} + U \dfrac{\partial}{\partial z}\right) B_r$ (c)
rotating spherical shell	Either $$\left(\dfrac{\partial}{\partial \theta} \sin\theta \dfrac{\partial}{\partial \theta} \sin\theta + \dfrac{\partial^2}{\partial \phi^2}\right) [\![H_\phi]\!] = -\sigma_s \alpha \sin\theta \dfrac{\partial}{\partial \phi} \left(\dfrac{\partial}{\partial t} + \Omega \dfrac{\partial}{\partial \phi}\right) B_r \quad \text{(d)}$$ or $$\left(\dfrac{\partial}{\partial \theta} \sin\theta \dfrac{\partial}{\partial \theta} \sin\theta + \dfrac{\partial^2}{\partial \phi^2}\right) [\![H_\theta]\!] = -\sigma_s \alpha \dfrac{\partial}{\partial \theta} \left[\sin^2\theta \left(\dfrac{\partial}{\partial t} + \Omega \dfrac{\partial}{\partial \phi}\right) B_r\right] \quad \text{(e)}$$

Finally, the jump condition implied by Ampère's law relates $\vec{K}_f$ to the fields (Eq. 2.10.21):

$$\vec{n} \times [\![\vec{H}]\!] = \vec{K}_f \tag{4}$$

These last three equations combine to provide a description of how the magnetic field diffuses through conductors of arbitrary geometry. Four typical geometries and associated boundary conditions are summarized in Table 6.3.1. The derivation of each of these conditions follows the steps now carried out in Cartesian coordinates.

<u>Translating Planar Sheet</u>: In this case, $B_n = B_x$ and $\vec{v} = U\vec{i}_y$. Then, Eqs. 2 and 3 become

$$\frac{\partial K_z}{\partial y} - \frac{\partial K_y}{\partial z} = -\sigma_s\left(\frac{\partial B_x}{\partial t} + U \frac{\partial B_x}{\partial y}\right) \tag{5}$$

$$\frac{\partial K_y}{\partial y} + \frac{\partial K_z}{\partial z} = 0 \tag{6}$$

Of the variables K_y and K_z, the latter is the more convenient. Hence, with the objective of eliminating K_y between these questions, $\partial/\partial y$ is taken of Eq. 5 and $\partial/\partial z$ is taken of Eq. 6 to generate a cross derivative that can be eliminated between these equations. Thus, Eqs. 5 and 6 become

$$\left(\frac{\partial^2}{\partial y^2} + \frac{\partial^2}{\partial z^2}\right) K_z = -\sigma_s \frac{\partial}{\partial y}\left(\frac{\partial}{\partial t} + U \frac{\partial}{\partial y}\right) B_x \tag{7}$$

Finally, Eq. 4 is used to write Eq. 7 as the required boundary condition, Eq. (a) of Table 6.3.1.

6.4 Magnetic Induction Motors and a Tachometer

A developed model for the rotating machine, shown in Fig. 6.4.1a, is detailed by Fig. 6.4.1b. It incorporates a stator structure much like that for a synchronous machine, for example the smooth air gap machine of Sec. 4.7. The windings shown here however have two rather than three phases, backed by a highly permeable magnetic material. The rotor also consists of a highly permeable material, but having its windings replaced by a sheet of conducting material wrapped on its periphery.

What makes this an induction machine is that the rotor currents are induced rather than imposed by means of windings and terminal pairs. The stator currents produce a magnetic flux density that has a component normal to the conducting sheet. Application of the integral induction law and Ohm's law (Eq. 6.2.4) to a surface lying in the plane of the sheet shows that circulating currents are induced in the sheet. These tend to produce their own fields and hence limit the normal flux density in the sheet. With the rotor assumed very long in the z direction compared to the rotor diameter, these sheet currents are modeled as mainly z-directed, closing in circulating paths on perfectly conducting "shorts" at $z=\pm\infty$.
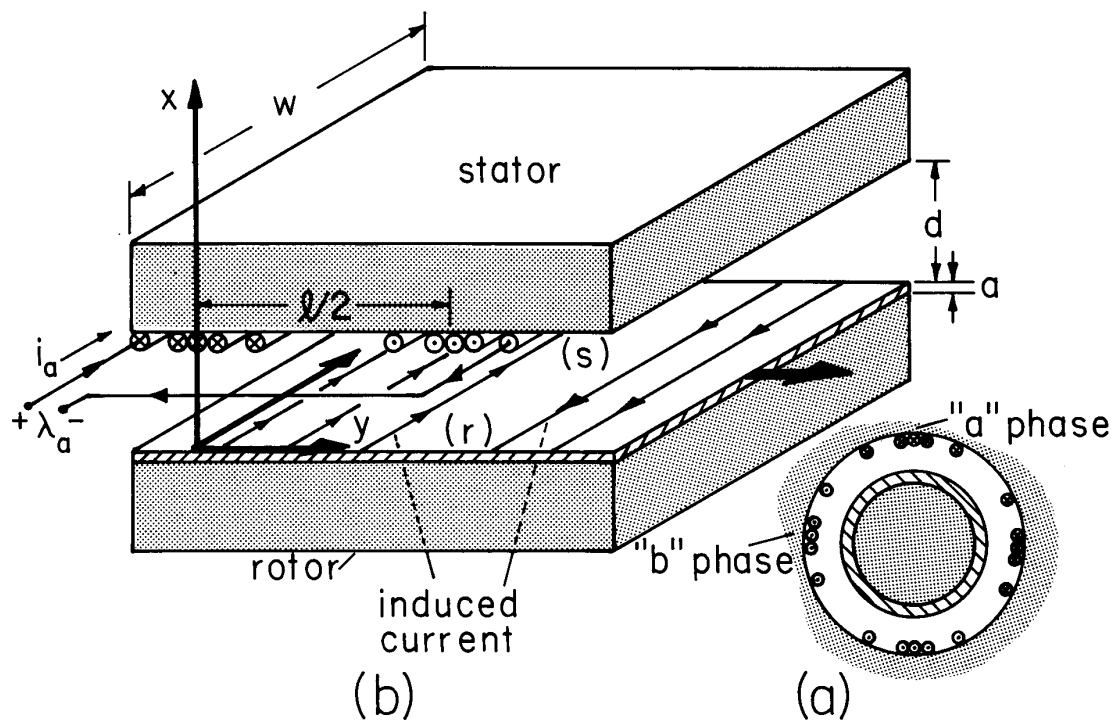

Fig. 6.4.1. (a) Cross section of rotating induction machine with thin-sheet conductor on rotor. (b) Developed model for (a) with air gap d and sheet conductor of thickness a. One of two phases on the stator is shown.

Viewed in terms of lumped parameter models, the induction machine is often represented by a conservative electromechanical coupling, such as developed for the synchronous machine in Sec. 4.7, with the rotor terminals shorted by resistors. In fact, some induction machines are constructed with wound rotors that can be connected to variable resistances through slip rings. However, most induction machines are made inherently more rugged by letting the currents flow through solid conductors, not windings. An important point made by the field representation used in this section is that the thin sheet model is in fact equivalent to the lumped parameter model, provided that the rotor is modeled by a properly distributed polyphase winding with equal resistances connected to each winding. But, if the sheet has finite thickness, the circuit model is not equivalent, as will be evident in Sec. 6.6.

Two-Phase Stator Currents: There are two windings on the stator, each with a sinusoidal distribution of turns density. The "b" phase is displaced by 90° relative to the "a" phase. Because magnetic induction depends explicitly on time rates of change, the description is one in terms of temporal comple

amplitudes. Hence, the stator current is modeled as being the surface current,

$$K_z^s = \text{Re}[\hat{i}_a e^{j\omega t} N_a \cos ky + \hat{i}_b e^{j\omega t} N_b \cos k(y - \tfrac{\ell}{4})] \tag{1}$$

where N_s and N_b are the peak turns per unit length on the respective phases and ℓ is the wavelength in the y-direction. For a two-pole rotating machine, ℓ is the rotor circumference. The complex amplitudes of the electrical terminal currents are $(\hat{i}_a, \hat{i}_b)$.

By using Euler's formula, $\cos \theta = (e^{j\theta} + e^{-j\theta})/2$, the cosines in Eq. 1 are written in terms of exponentials so that the surface current takes the alternative form

$$K_z^s = \text{Re}[\hat{K}_+^s e^{j(\omega t - ky)} + \hat{K}_-^s e^{j(\omega t + ky)}] \tag{2}$$

where
$$\hat{K}_{\pm}^s = \tfrac{1}{2}(\hat{i}_a N_a + \hat{i}_b N_b e^{\pm \frac{jk\ell}{4}})$$

Thus, the excitation is written in the form of a complex amplitude Fourier series. This type of representation is discussed in Sec. 5.16. In general, the series takes the form of Eq. 5.16.1. In the case at hand, there are only two terms, n = 1 (k_1 = k) and n = -1 (k_{-1} = -k), corresponding physically to waves propagating in the + and -z directions.

The fields satisfy linear bulk and boundary equations. Hence, the response to Eq. 2 is the superposition of the response to the first term and a response to the second, found from the first by simply replacing $\hat{K}_+^s \to \hat{K}_-^s$ and $k \to -k$.

<u>Fields</u>: Because the flux linkages are to be computed, it is convenient to describe the air-gap fields in terms of the vector potential, $\vec{A} = A\vec{i}_z$, the Cartesian coordinate case of Table 2.18.1; thus, $\hat{B}_x = -jkA$. In view of the "infinitely" permeable stator and rotor materials, boundary conditions on single complex amplitudes of the fields at the stator and rotor surfaces follow from Ampère's law (Eq. 2.10.21). The boundary condition at the stator is thus

$$\hat{H}_y^s = -\hat{K}^s \tag{3}$$

and the composite boundary condition for the thin sheet, Eq. (a) of Table 6.3.1 with $\partial/\partial z = 0$, is

$$\hat{H}_y^r = \frac{\sigma_s}{k}(\omega - kU)\hat{B}_x^r = \frac{\sigma_s}{k}(\omega - kU)(-jk\hat{A}^r) \tag{4}$$

Fields at the stator and rotor surfaces are related by the transfer relations (b) of Table 2.19.1:

$$\begin{bmatrix} \hat{A}^s \\ \\ \hat{A}^r \end{bmatrix} = \frac{\mu_o}{k} \begin{bmatrix} -\coth(kd) & \dfrac{1}{\sinh(kd)} \\ \\ \dfrac{-1}{\sinh(kd)} & \coth(kd) \end{bmatrix} \begin{bmatrix} \hat{H}_y^s \\ \\ \hat{H}_y^r \end{bmatrix} \tag{5}$$

With the objective of finding $\hat{H}_y^r$, which by Ampere's law is the rotor surface current, these last three equations are now combined. Equation 4 (solved for $\hat{A}^r$) and Eq. 3 are substituted into Eq. 5b. This expression is then solved for $\hat{H}_y^r$:

$$\hat{H}_{y\pm}^r = - \frac{\hat{K}_+^s S_{m\pm}[j + S_{m\pm}\coth(kd)]}{\sinh(kd)[1 + S_{m\pm}^2 \coth^2(kd)]} \tag{6}$$

The dimensionless number S_m combines the ratio of a magnetic diffusion time $\tau_m = \mu_o \sigma_s/k$ to the characteristic time $1/\omega$ and a magnetic Reynolds number $\mu_o \sigma_s U$:

$$S_{m\pm} \equiv \frac{\mu_o \sigma_s}{k}(\omega \mp kU) \tag{7}$$

In writing Eq. 6, the components induced by the respective traveling waves of Eq. 2 are identified by replacing $\hat{K}^s \to \hat{K}_{\pm}^s$ and $k \to \pm k$. Note that coth(kd) and sinh(kd) are odd functions.

Time-Average Force: To determine the force of magnetic origin acting in the y direction on the rotor, the appropriate volume of integration is as shown in Fig. 4.2.1a. The only contribution to the integration of the stress over the enclosing surface comes from S_1, here taken as a surface adjacent to the rotor. It then follows from Eq. 5.16.4 that the time-average rotor force is simply

$$\left\langle f_y \right\rangle_t = \left(\frac{p}{2} \ell w\right) \frac{1}{2} \, \text{Re}[\hat{B}^r_{x+}(\hat{H}^r_{y+})^* + \hat{B}^r_{x-}(\hat{H}^r_{y-})^*] \tag{8}$$

where w is the rotor length in the z direction and p is the number of poles (the number of half-wave-lengths). Hence, $p\ell/2$ is the total rotor length in the y direction.

In Eq. 8, $\hat{B}^r_{x\pm} = \mp jk\hat{A}^r_\pm$, where $\hat{A}^r_\pm$ follow from Eqs. 3 and 5b:

$$\hat{A}^r_\pm = \frac{\mu_o}{k} \left[\frac{\hat{K}^s_\pm}{\sinh(kd)} + \coth(kd)\hat{H}^r_{y\pm}\right] \tag{9}$$

Thus, substitution for $\hat{B}^r_{x\pm}$ in Eq. 8 exploits the fact that self-fields can make no contribution to the total force to express the force as an interaction between stator and rotor surface currents:

$$\left\langle f_y \right\rangle_t = -\frac{p\ell w}{4} \frac{\mu_o}{\sinh(kd)} \, \text{Re}[j\hat{K}^s_+(\hat{H}^r_{y+})^* - j\hat{K}^s_-(\hat{H}^r_{y-})^*] \tag{10}$$

In terms of stator currents, Eq. 6 serves to evaluate this time-average force:

$$\left\langle f_y \right\rangle_t = \frac{p\ell w\mu_o}{4\sinh^2(kd)} \left[\frac{S_{m+}|\hat{K}^s_+|^2}{1 + S^2_{m+}\coth^2(kd)} - \frac{S_{m-}|\hat{K}^s_-|^2}{1 + S^2_{m-}\coth^2(kd)}\right] \tag{11}$$

Balanced Two-Phase Fields and Time-Average Force: The stator currents become a pure traveling wave if the (b) phase is made to temporally lag the (a) phase by 90°, and the windings have the same peak turns densities. Formally, this is seen from the definitions of $\hat{K}^s_\pm$ given with Eq. 2:

$$\begin{array}{ccc}
\hat{i}_b = \hat{i}_a e^{-j\pi/2} & & \hat{K}^s_+ = \hat{i}_a N_a \\
& \Longrightarrow & \\
N_a = N_b & & \hat{K}^s_- = 0
\end{array} \tag{12}$$

Only the first term in Eq. 11 contributes to the force. The dependence of this force on S_{m+} is familiar from the electroquasistatic analogue developed in Sec. 5.13. In Fig. 6.4.2a, the force is shown as a function of the material velocity divided by the traveling-wave phase velocity ω/k. Given the dependence of the force on S_{m+}, this plot is the result of first shifting the origin so that $S_{m+} = 0$ where $\omega = kU$ and then "flipping" the plot about the vertical axis passing through this origin.

The parameter S_{m+} is the effective magnetic diffusion time multiplied by the angular frequency $(\omega-kU)$ for an observer moving with the conducting sheet. The force is in the same direction as the traveling wave, provided S_{m+} is positive so that the traveling wave has a speed greater than that of the material. To understand the force-speed diagram, consider the phase relationship between stator and rotor surface currents, implied by Eq. 6 ($H_y = K_z$). For near synchronism between traveling wave and material, (i) typifies the operating point. In Eq. 6, small S_{m+} implies the complex amplitude (i) shown in the phase diagram of Fig. 6.4.2b. At a given instant, the rotor current spatially lags that on the stator by slightly more than 90°, as sketched in inset (i) of Fig. 6.4.2a. This current has just the right distribution for producing a force to the right, but because S_m is small (the time rate of change in a frame moving with the materials is small) the induced current is small. The magnetic field is distributed essentially as if there were no rotor current. Increasing S_m improves the magnitude of the current but at the price of compromising the relative spatial phase. The ultimate compromise between phase and magnitude comes at (ii) where $S_m = \tanh(kd)$. As S_m becomes large, currents in the rotor completely shield out the normal magnetic field. The rotor current becomes as large as is possible, but the spatial phase relation is wrong for producing a force in the y direction. Operating point (iii) is approaching this condition, with the magnetic field approximating that for a perfectly conducting sheet.

Electrical Terminal Relations: To compute the voltages (v_a, v_b) required to produce the terminal currents (i_a, i_b), the flux linkages (λ_a, λ_b) must be determined. For example, consider the (a) phase of a two-pole machine. The windings carrying current in the z direction at y' and returning the current at $y' + \ell/2$ each link a magnetic flux (Eq. (f) of Table 2.18.1):
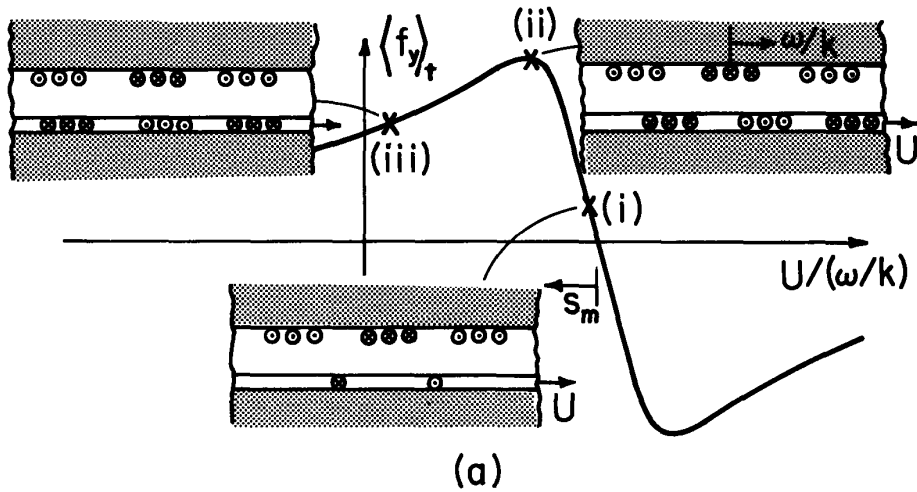
Fig. 6.4.2. (a) Time-average force for induction
machine of Fig. 6.4.1 with balanced two-phase
excitation. Abscissa is material velocity
relative to wave phase velocity. The slip is
$s_m \equiv S_{m+}/(\mu_0\sigma_s\omega/k)$. Insets show spatial
phase of stator and rotor currents at a given
instant. (b) Phasor $\hat{H}_y^r$, showing effect of in-
creasing S_m on the phase and amplitude. Oper-
ating points (i) → (iii) are shown in (a). In
nomenclature of lumped parameter induction
machines, (i) is resistance dominated operation
while (iii) is reactance dominated.
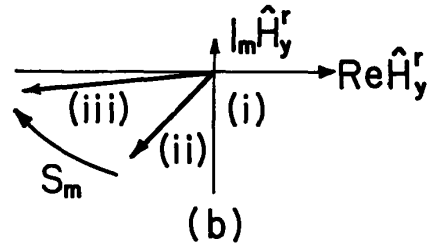
$$\Phi_\lambda = w[A^s(y') - A^s(y' + \ell/2)] \tag{13}$$

Written as the superposition of the two field components, so that the dependence on y' is explicit, this
expression becomes ($k \equiv 2\pi/\ell$)

$$\Phi_\lambda = wRe[\hat{A}_+^s e^{j(\omega t - ky')} + \hat{A}_-^s e^{j(\omega t + ky')} - \hat{A}_+^s e^{-j\pi}e^{j(\omega t - ky')} - \hat{A}_-^s e^{j\pi}e^{j(\omega t + ky')} \tag{14}$$

$$= wRe2(\hat{A}_+^s e^{-jky'} + \hat{A}_-^s e^{jky'})e^{j\omega t}$$

In the interval dy' in the neighborhood of y = y' there are $N_a \cos ky'\, dy'$ turns, so the flux linked by
the (a) phase is altogether

$$\lambda_a = \int_{-\ell/4}^{\ell/4} \Phi_\lambda(y')N_a \cos ky'\, dy' = wN_a Re \int_{-\ell/4}^{\ell/4} (\hat{A}_+^s e^{-jky'} + \hat{A}_-^s e^{jky'})(e^{jky'} + e^{-jky'})e^{j\omega t}dy' \tag{15}$$

Only the constant terms contribute to the integration, and substitution for $\hat{A}_\pm^s$ from Eq. 5a gives

$$\lambda_a = \frac{w\ell}{2}\frac{N_a}{k}\mu_0 Re\left[\coth(kd)(\hat{K}_+^s + \hat{K}_-^s) + \frac{(\hat{H}_{y+}^r + \hat{H}_{y-}^r)}{\sinh(kd)}\right]e^{j\omega t} \tag{16}$$

Remember that $K_\pm^s$ are given functions of the terminal currents, Eq. 2. Thus, $\hat{H}_{y\pm}^r$ are also given as
a function of the terminal currents by Eq. 6 and Eq. 16 is the required (a) phase terminal relation
$\lambda_a(i_a, i_b)$. The same line of reasoning shows that λ_b is given by Eq. 16 with $N_a \to -jN_b$, $\hat{K}_+^s + \hat{K}_-^s \to \hat{K}_+^s - \hat{K}_-^s$
and $\hat{H}_{y+}^r + \hat{H}_{y-}^r \to \hat{H}_{y+}^r - \hat{H}_{y-}^r$.

$$L_1 \equiv L_2 \equiv \frac{wN_a^2 \ell^2 \mu_o}{4\pi} \tanh \left(\frac{\pi d}{\ell}\right)$$

$$M \equiv \frac{wN_a^2 \ell^2 \mu_o}{4\pi \sinh \left(\frac{2\pi d}{\ell}\right)} \quad ; \quad R \equiv \frac{\ell w N_a^2}{2\sigma_s}$$

$$s_m \equiv \text{"slip"} = (1 - \frac{kU}{\omega}) = S_{m+}/(\mu_o \sigma_s \omega/k)$$
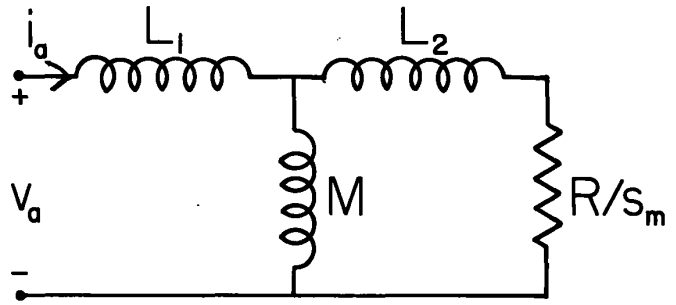

Fig. 6.4.3. Equivalent circuit for balanced operation of induction machine.

Balanced Two-Phase Equivalent Circuit: With excitations as summarized by Eq. 12, the terminal voltage on the (a) phase follows from Eq. 16 as

$$\hat{v}_a = j\omega\hat{\lambda}_a = j\omega \frac{w\ell N_a^2 \mu_o}{2k} \left[\coth kd - \frac{S_{m+}[j + S_{m+}\coth(kd)]}{\sinh^2 kd (1+S_{m+}^2 \coth^2 kd)} \right] \hat{i}_a \tag{17}$$

This relation of voltage and current is the same as is obtained for the circuit of Fig. 6.4.3. The parameter S_{m+}, normalized to a magnetic Reynolds number based on the wave velocity ω/k, is what is conventionally defined as the "slip," s_m.

Single-Phase Machine: With only the (a) phase excited, positive and negative traveling waves result having equal magnitudes. According to Eq. 2,

$$i_b = 0 \Rightarrow \hat{K}_+^s = \hat{K}_-^s = \frac{1}{2} N_a \hat{i}_a \tag{18}$$

The time-average force, Eq. 11, is the superposition of the forces that would be induced by purely forward and backward traveling waves. The resulting force-speed characteristic, sketched in Fig. 6.4.4, is rigorously the sum of the time-average forces from the traveling-wave components. At zero speed, these forces cancel. Provided the slope of the characteristic at zero speed is positive, once started in either direction, the rotor experiences a force tending to further increase the velocity. It follows from Eq. 11 that at $U = 0$ the slope is

$$\frac{d\langle f_y \rangle_t}{dU} = \frac{p\ell wN_a^2 |i_a|^2}{8 \sinh^2 kd} \frac{k}{\omega} R_M \frac{(R_M^2 \coth^2 kd - 1)}{(1 + R_M^2 \coth^2 kd)^2}; \quad R_M \equiv \mu_o \sigma_s \omega/k \tag{19}$$

so the slope is positive, provided the frequency is high enough to make $R_M > \tanh(kd)$.
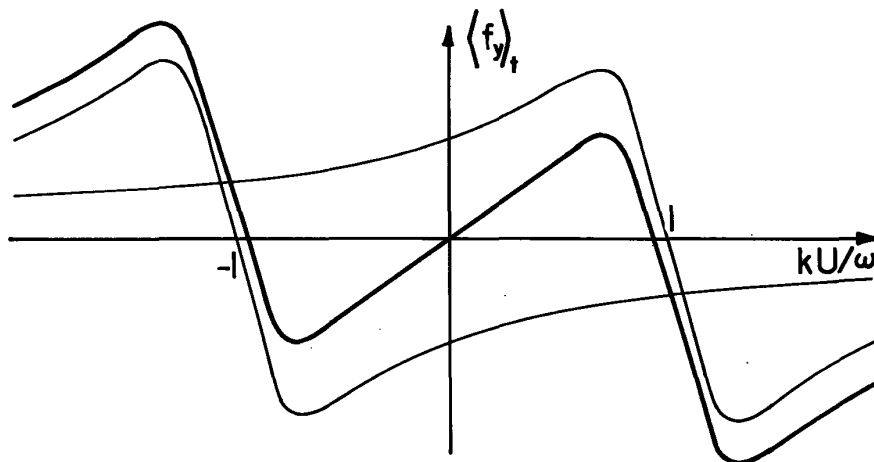

Fig. 6.4.4. Time-average force for single-phase induction machine as function of material velocity normalized to wave velocity. Total force is superposition of forces due to forward and backward wave components.

In practice, single-phase induction machines are started by pole shading or by using a (b) winding connected to the excitation in such a way that a temporal phase shift takes place, perhaps by a capacitor. Under start conditions, one force component then dominates the other.[1]
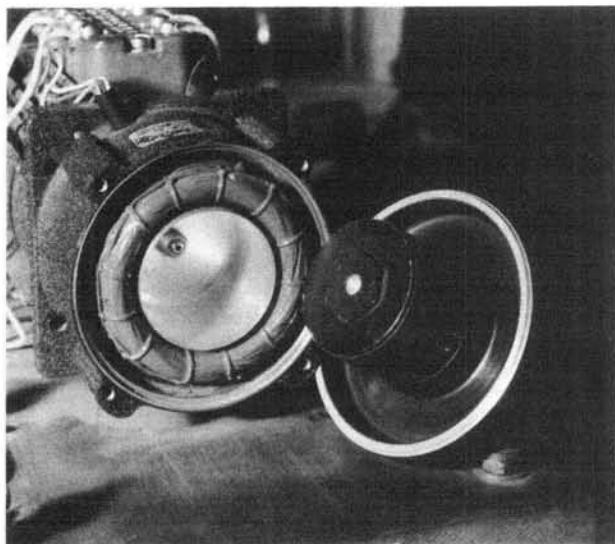

Fig. 6.4.5

Drag-cup tachometer with end cap and attached magnetic core removed so that thin-walled rotating cup is visible. The core is the lower highly permeable rotor material in Fig. 6.4.1, the cup is the moving conducting sheet. Coils adjacent to the cup rim are the stator windings. In this example the core is actually fixed and there is an appreciable air gap between core and cup.

Tachometer: One common way in which the induction machine sees application as a generator is for speed measurement. As a rotating machine, the model pertains to the drag-cup tachometer shown in Fig. 6.4.5. In linear geometry, the induction interaction might be used to measure the velocity of a moving conducting sheet. Single phase excitation, say of the (b) phase, is equivalent to a standing-wave excitation. With no motion, currents induced in the sheet also form a standing wave in spatial phase with the excitation. Material motion induces an imbalance in the forward and backward wave components. Thus, with no motion no signal is detected on the (a) phase, but with motion there is a sinusoidal signal at the frequency ω. The magnetic interaction exploited here is the analogue of that discussed for an electroquasistatic interaction in connection with Figs. 5.13.3 and 5.13.4.

With single phase excitation of the (b) phase, $\hat{i}_a = 0$ and according to Eq. 2, $\hat{K}^s_\pm = \mp \frac{1}{2} \hat{i}_b N_b$. The voltage on the (a) phase follows from Eq. 16:

$$\hat{v}_a = j\omega\hat{\lambda}_a = -j \frac{\omega w \ell N_a N_b \mu_o \hat{i}_b}{4k \sinh^2 kd} \left(\frac{S_{m+}}{1 + jS_{m+} \coth kd} - \frac{S_{m-}}{1 + jS_{m-} \coth kd} \right) \tag{20}$$

As expected, the output voltage is zero if $U = 0$ ($S_{m+} = S_{m-}$). The dependence of v_a on the velocity can be used to measure U. For example, the amplitude of the output follows from Eq. 20 as

$$|\hat{v}_a| = \frac{v_o \left[\frac{\mu_o \sigma_s \omega}{k} \right] [kU/\omega]}{\sqrt{(1 + S^2_{m+} \coth^2 kd)(1 + S^2_{m-} \coth^2 kd)}} \tag{21}$$

where

$$v_o \equiv \frac{\omega w \ell N_a N_b \mu_o}{2k \sinh kd \coth kd} ; \quad S_{m\pm} \equiv \frac{\mu_o \sigma_s}{k} (\omega \mp kU)$$
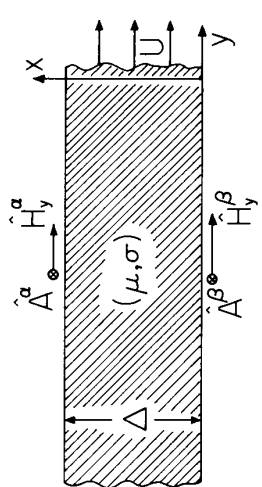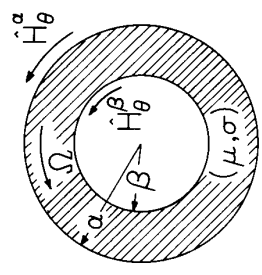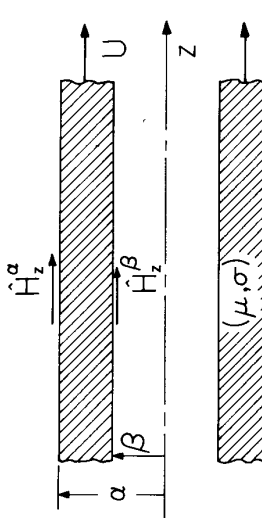
The analogy to the electroquasistatic tachometer of Sec. 5.13 is emphasized by the direct correspondence between Eqs. 20 and 5.13.15, and between Eqs. 21 and 5.13.16. The dependence on U given by Eq. 21 is illustrated by Fig. 5.13.5.

6.5 Diffusion Transfer Relations for Materials in Uniform Translation or Rotation

In terms of the vector potential $\vec{A}$, discussed in Sec. 2.18, magnetic diffusion in regions having uniform permeability and conductivity is described by Eq. 6.2.6 with $\vec{B} = \nabla \times \vec{A}$ and $\nabla \cdot \vec{A} = 0$:

1. For a description of induction machines in lumped-parameter terms, see H. H. Woodson and J. R. Melcher, Electromechanical Dynamics, Pt. I, John Wiley & Sons, New York, 1968, pp. 127-140; also, A. E. Fitzgerald, C. Kingsley, and A. Kusko, Electrical Machinery, McGraw-Hill Book Company, New York, 1971, pp. 525-531; S. A. Nasar and I. Boldea, Linear Motion Electric Machines, John Wiley and Sons, New York, 1976.

Table 6.5.1. Magnetic diffusion transfer relations with translation or rotation.

Planar layer	Rotating cylinder	Translating cylinder

Planar layer

$$\vec{A} = \vec{i}_z \,\mathrm{Re}\,\hat{A}(x)\, \exp j(\omega t - ky)$$

(a)
$$\begin{bmatrix} \hat{H}_y^\alpha \\ \hat{H}_y^\beta \end{bmatrix} = \frac{\gamma}{\mu} \begin{bmatrix} -\coth\gamma\Delta & \dfrac{1}{\sinh\gamma\Delta} \\[2mm] \dfrac{-1}{\sinh\gamma\Delta} & \coth\gamma\Delta \end{bmatrix} \begin{bmatrix} \hat{A}^\alpha \\ \hat{A}^\beta \end{bmatrix}$$

(b)
$$\begin{bmatrix} \hat{A}^\alpha \\ \hat{A}^\beta \end{bmatrix} = \frac{\mu}{\gamma} \begin{bmatrix} -\coth\gamma\Delta & \dfrac{1}{\sinh\gamma\Delta} \\[2mm] \dfrac{-1}{\sinh\gamma\Delta} & \coth\gamma\Delta \end{bmatrix} \begin{bmatrix} \hat{H}_y^\alpha \\ \hat{H}_y^\beta \end{bmatrix}$$

$$\gamma \equiv \sqrt{k^2 + j\mu\sigma(\omega - kU)}$$

$$\begin{bmatrix} \hat{A}^\alpha \\ \hat{A}^\beta \end{bmatrix} = \frac{j}{k} \begin{bmatrix} \hat{B}_x^\alpha \\ \hat{B}_x^\beta \end{bmatrix}$$

Rotating cylinder

$$\vec{A} = \vec{i}_z \,\mathrm{Re}\,\hat{A}(r)\, \exp j(\omega t - m\theta)$$

(c)
$$\begin{bmatrix} \hat{H}_\theta^\alpha \\ \hat{H}_\theta^\beta \end{bmatrix} = \frac{1}{\mu} \begin{bmatrix} f_m(\beta,\alpha,\gamma) & g_m(\alpha,\beta,\gamma) \\ g_m(\beta,\alpha,\gamma) & f_m(\alpha,\beta,\gamma) \end{bmatrix} \begin{bmatrix} \hat{A}^\alpha \\ \hat{A}^\beta \end{bmatrix}$$

(d)
$$\begin{bmatrix} \hat{A}^\alpha \\ \hat{A}^\beta \end{bmatrix} = \mu \begin{bmatrix} F_m(\beta,\alpha,\gamma) & G_m(\alpha,\beta,\gamma) \\ G_m(\beta,\alpha,\gamma) & F_m(\alpha,\beta,\gamma) \end{bmatrix} \begin{bmatrix} \hat{H}_\theta^\alpha \\ \hat{H}_\theta^\beta \end{bmatrix}$$

f_m, g_m, F_m and G_m as defined in Table 2.16.2 with $k \to \gamma$ where

$$\gamma \equiv \sqrt{j\mu\sigma(\omega - m\Omega)}$$

$$\begin{bmatrix} \hat{A}^\alpha \\ \hat{A}^\beta \end{bmatrix} = \frac{j}{m} \begin{bmatrix} \alpha\hat{B}_r^\alpha \\ \beta\hat{B}_r^\beta \end{bmatrix}$$

Translating cylinder

$$\vec{A} = \vec{i}_\theta \hat{A}_\theta(r)\, \exp j(\omega t - kz)$$

(e)
$$\begin{bmatrix} \hat{H}_z^\alpha \\ \hat{H}_z^\beta \end{bmatrix} = -\frac{\gamma^2}{\mu} \begin{bmatrix} F_o(\beta,\alpha,\gamma) & G_o(\alpha,\beta,\gamma) \\ G_o(\beta,\alpha,\gamma) & F_o(\alpha,\beta,\gamma) \end{bmatrix} \begin{bmatrix} \dfrac{\hat{\Lambda}^\alpha}{\alpha} \\[2mm] \dfrac{\hat{\Lambda}^\beta}{\beta} \end{bmatrix}$$

(f)
$$\begin{bmatrix} \dfrac{\hat{\Lambda}^\alpha}{\alpha} \\[2mm] \dfrac{\hat{\Lambda}^\beta}{\beta} \end{bmatrix} = -\frac{\mu}{\gamma^2} \begin{bmatrix} f_o(\beta,\alpha,\gamma) & g_o(\alpha,\beta,\gamma) \\ g_o(\beta,\alpha,\gamma) & f_o(\alpha,\beta,\gamma) \end{bmatrix} \begin{bmatrix} \hat{H}_z^\alpha \\ \hat{H}_z^\beta \end{bmatrix}$$

F_o, G_o, f_o and g_o as defined in Table 2.16.2 with $k \to \gamma$ where

$$\gamma \equiv \sqrt{k^2 + j\mu\sigma(\omega - kU)}$$

$$\begin{bmatrix} \dfrac{\hat{\Lambda}^\alpha}{\alpha} \\[2mm] \dfrac{\hat{\Lambda}^\beta}{\beta} \end{bmatrix} = -\frac{j}{k} \begin{bmatrix} \hat{B}_r^\alpha \\ \hat{B}_r^\beta \end{bmatrix}$$

$$\nabla \times \left[\frac{1}{\mu\sigma} \nabla \times (\nabla \times \vec{A}) + \frac{\partial \vec{A}}{\partial t} - \vec{v} \times (\nabla \times \vec{A})\right] = 0 \tag{1}$$

Because the curl of the gradient of any scalar, say $-\Phi$, is zero, a solution to this equation is

$$\frac{1}{\mu\sigma} \nabla \times (\nabla \times \vec{A}) + \frac{\partial \vec{A}}{\partial t} - \vec{v} \times (\nabla \times \vec{A}) = -\nabla\Phi \tag{2}$$

For a given material motion, this equation is linear in $\vec{A}$ so that solutions can be superimposed. The inhomogeneous solutions resulting from the "drive" on the right can be added to the homogeneous solutions satisfying Eq. 2 with $\Phi = 0$. A vector identity* converts the latter equation to

$$\frac{1}{\mu\sigma} \nabla^2\vec{A} = \frac{\partial \vec{A}}{\partial t} - \vec{v} \times (\nabla \times \vec{A}) \tag{3}$$

where the vector Laplacian must be distinguished from its scalar counterpart (Appendix A). This section is devoted to developing certain useful solutions to Eq. 3 in such a form that they can be used in problem solving. The geometries to be treated, summarized in Table 6.5.1, are extensions of those identified in Sec. 2.19, two-dimensional or symmetric configurations where the vector potential has a single component.

Planar Layer in Translation: In Cartesian coordinates, with $\vec{A} = A(x,y)\vec{i}_z$ and the material moving uniformly in the y direction, so that $\vec{v} = U\vec{i}_y$, Eq. 3 reduces to its z component, which is

$$\frac{1}{\mu\sigma} \nabla^2 A = \frac{\partial A}{\partial t} + U \frac{\partial A}{\partial y} \tag{4}$$

With solutions taking the complex-amplitude form $A(x,y,t) = Re\hat{A}(x)\exp j(\omega t - ky)$, this equation reduces to

$$\frac{d^2\hat{A}}{dx^2} - \gamma^2\hat{A} = 0; \quad \gamma^2 \equiv k^2 + j\mu\sigma(\omega - kU) \tag{5}$$

Transfer relations can now be deduced following the same line of reasoning used in preceding from Eq. 2.16.13 to the relations of Table 2.16.1, or from Eq. 2.19.3 to the Cartesian relations of Table 2.19.1. With $(\hat{A}^\alpha, \hat{A}^\beta)$ the complex amplitudes at $x = \Delta$ and $x = 0$, respectively, the solution to Eq. 5 is:

$$\hat{A} = \hat{A}^\alpha \frac{\sinh \gamma x}{\sinh \gamma\Delta} - \hat{A}^\beta \frac{\sinh \gamma(x-\Delta)}{\sinh \gamma\Delta} \tag{6}$$

Evaluation of $\hat{H}_y = -(1/\mu)d\hat{A}/dx$ (Table 2.18.1) at $x = \Delta$ and $x = 0$ then gives the transfer relations, Eqs. (a) of Table 6.5.1. Inversion of these relations gives Eqs. (b). Note that $\gamma = \gamma_r + j\gamma_i$ in Eq. 6. Thus,

$$\sinh \gamma x = \sinh(\gamma_r x + j\gamma_i x) = \sinh \gamma_r x \cos \gamma_i x + j \cosh \gamma_r x \sin \gamma_i x \tag{7}$$

is a complex function. In computer libraries it is usually the circular rather than the hyberbolic functions that are provided with the capability of having complex arguments. Then, evaluation is accomplished by replacing $\sinh \gamma x \rightarrow -j \sin j\gamma x$ in Eq. 6.

The diffusion transfer relations are the same as those for a nonconducting region (Table 2.19.1), except that k is replaced by γ. The transverse wavenumber governs the manner and degree of penetration of the field into the conductor, and is examined in Sec. 6.6. The transfer relations for a planar region are applied in Secs. 6.6-6.8 and 6.10.

Rotating Cylinder: In a material suffering rigid-body rotation with the angular velocity Ω, the velocity is $\vec{v} = \Omega r \vec{i}_\theta$. For field dynamics not depending on z, the appropriate form is $\vec{A} = A(r,\theta,t)\vec{i}_z$, the polar coordinate case of Table 2.18.1. Then, Eq. 3 reduces to its z component:

$$\frac{1}{\mu\sigma} \nabla^2 A = \frac{\partial A}{\partial t} + \Omega \frac{\partial A}{\partial \theta} \tag{8}$$

Substitution of $A = Re\hat{A}(r) \exp j(\omega t - m\theta)$ reduces this expression to

---

* $\nabla \times (\nabla \times \vec{A}) = \nabla(\nabla \cdot \vec{A}) - \nabla^2\vec{A}$

$$\frac{d^2\hat{A}}{dr^2} + \frac{1}{r}\frac{d\hat{A}}{dr} - (\gamma^2 + \frac{m^2}{r^2})\hat{A} = 0; \quad \gamma^2 \equiv j\mu\sigma(\omega - m\Omega) \tag{9}$$

With the identification $k^2 \rightarrow \gamma^2$, Eq. 9 is Eq. 2.16.19, Bessel's equation. The appropriate solution for the cylindrical annulus shown in Table 6.5.1, with outer and inner radii at $r = \alpha$ and $r = \beta$, respectively, takes the same form as Eq. 2.16.25:

$$\hat{A} = \hat{A}^\alpha \frac{[H_m(j\gamma\beta)J_m(j\gamma r) - J_m(j\gamma\beta)H_m(j\gamma r)]}{[H_m(j\gamma\beta)J_m(j\gamma\alpha) - J_m(j\gamma\beta)H_m(j\gamma\alpha)]}$$

$$+ \hat{A}^\beta \frac{[J_m(j\gamma\alpha)H_m(j\gamma r) - H_m(j\gamma\alpha)J_m(j\gamma r)]}{[J_m(j\gamma\alpha)H_m(j\gamma\beta) - H_m(j\gamma\alpha)J_m(j\gamma\beta)]} \tag{10}$$

Evaluation of $H_\theta = -(1/\mu)d\hat{A}/dr$ (see Table 2.18.1) at the respective surfaces then gives the transfer relations (c) of Table 6.5.1. Inversion of these relations results in Eqs. (d).

The entries appearing in these transfer relations are those used to represent Laplacian fields, defined in Table 2.16.2, except that k is replaced by γ. In modeling a configuration composed of two or more regions having differing values of $\mu\sigma$, it is necessary to distinguish among two or more values of γ. By agreement, if the third argument is simply k, it is suppressed. For example,

$$f_m(x,y,k) \equiv f_m(x,y) \tag{11}$$

so that the transfer relation entries introduced in this section are natural generalizations of those introduced in Sec. 2.16.

Bessel and Hankel functions of complex argument bear much the same relationship to the real-argumen limiting cases as do the circular functions in Cartesian coordinates. Computer library functions that allow complex arguments may be in terms of the Bessel function of second kind, N_m, in which case the definition of the Hankel function, Eq. 2.16.29, is used to evaluate H_m. For the rotating cylinder, the real and imaginary parts of the arguments are equal and, in this case, the Bessel and Hankel functions are tabulated as the Kelvin functions:[1]

$$ber_m x + jbei_m x \equiv J_m(e^{j3\pi/4}x)$$

$$ker_m x + jkei_m x \equiv \frac{j\pi}{2} H_m(e^{j3\pi/4}x) \tag{12}$$

Axisymmetric Translating Cylinder: To complete Table 6.5.1, consider the annular shaped material moving with a uniform velocity $\vec{v} = U\vec{i}_z$ in the axial direction under axisymmetric conditions. Then, the appropriate vector potential is $\vec{A} = \vec{i}_\theta A(r,z,t)$ and Eq. 3 becomes

$$\frac{1}{\mu\sigma}\{\frac{\partial}{\partial r}[\frac{1}{r}\frac{\partial}{\partial r}(rA)] + \frac{\partial^2 A}{\partial z^2}\} = \frac{\partial A}{\partial t} + U\frac{\partial A}{\partial z} \tag{13}$$

Substitution of $A = Re\hat{A}(r)\exp j(\omega t - kz)$ results in an equation of the same form as the homogeneous part of Eq. 2.19.9,

$$\frac{d^2\hat{A}}{dr^2} + \frac{1}{r}\frac{d\hat{A}}{dr} - (\gamma^2 + \frac{1}{r^2})\hat{A} = 0; \quad \gamma^2 \equiv k^2 + j\mu\sigma(\omega - kU) \tag{14}$$

where k^2 has been replaced by γ^2. Thus, the solution is Eq. 2.19.10 with $k \rightarrow \gamma$:

$$\hat{\Lambda} \equiv r\hat{A} = \hat{A}^\alpha \frac{[H_1(j\gamma\beta)rJ_1(j\gamma r) - J_1(j\gamma\beta)rH_1(j\gamma r)]}{[H_1(j\gamma\beta)J_1(j\gamma\alpha) - J_1(j\gamma\beta)H_1(j\gamma\alpha)]}$$

$$+ \hat{A}^\beta \frac{[J_1(j\gamma\alpha)rH_1(j\gamma r) - H_1(j\gamma\alpha)rJ_1(j\gamma r)]}{[J_1(j\gamma\alpha)H_1(j\gamma\beta) - H_1(j\gamma\alpha)J_1(j\gamma\beta)]} \tag{15}$$

---

1. M. Abramowitz and I. A. Stegun, Handbook of Mathematical Functions with Formulas, Graphs, and Mathematical Tables, U.S. Government Printing Office, Washington D.C., 1964, p. 379 and pp. 430-433.

The transfer Eqs. (e) of Table 6.5.1 follow by evaluating $H_z = (1/\mu r)\partial\Lambda/\partial r$ at the outer and inner radii. Identities, Eqs. 2.19.12 and 2.16.26c, are used to write the entries in terms of previously defined functions. The inverse relations are Eqs. (f).

6.6 Induction Motor with Deep Conductor: A Magnetic Diffusion Study

While also being of practical significance, the induction interaction considered in this section is chosen to give insights concerning sinusoidal steady-state magnetic diffusion into the bulk of uniform conductors. The model is similar to the thin-sheet developed model shown in Fig. 6.4, except that the rotor conductor now has a finite thickness, a, that can in general be comparable to the effective skin depth δ', to the wavelength $2\pi/k$ of the imposed traveling wave of surface current on the stator and to the air gap d. The revised cross section is shown in Fig. 6.6.1. With the understanding that various stator configurations could be represented as in Sec. 6.4, the stator current is taken as a pure traveling wave.

The configuration allows for an examination of the thin-sheet model of Sec. 6.3 while also placing in perspective the opposite extreme, the short skin-depth model introduced in Sec. 6.8. The sinusoidal steady-state driven response emphasized in this section is also related to the temporal modes of the system in Sec. 6.10.

In terms of the locations defined in Fig. 6.6.1, boundary and jump conditions represent Ampère's law (Eq. 2.10.21):

$$H_y^a = -\text{Re}\hat{K}_+^s e^{j(\omega t - ky)} \tag{1}$$

$$H_y^b = H_y^c \tag{2}$$

$$H_y^d = 0 \tag{3}$$

and continuity of magnetic flux density (Eq. 2.10.22),

$$B_x^b = B_x^c; \quad A^b = A^c \tag{4}$$

Fig. 6.6.1. Induction machine with rotor conductor having finite thickness a.

Identification of the bulk relations (b) of Table 6.5.1, first with the air gap and then with the conducting layer, gives

$$
\begin{bmatrix} \hat{A}^a \\ \hat{A}^b \end{bmatrix} = \frac{j}{k}\begin{bmatrix} \hat{B}_x^a \\ \hat{B}_x^b \end{bmatrix} = \frac{\mu_o}{k}\begin{bmatrix} -\coth(kd) & \dfrac{1}{\sinh(kd)} \\[2mm] \dfrac{-1}{\sinh(kd)} & \coth(kd) \end{bmatrix}\begin{bmatrix} -\hat{K}_+^s \\ \hat{H}_y^b \end{bmatrix} \tag{5}
$$

$$
\begin{bmatrix} \hat{A}^c \\ \hat{A}^d \end{bmatrix} = \frac{j}{k}\begin{bmatrix} \hat{B}_x^b \\ \hat{B}_x^d \end{bmatrix} = \frac{\mu}{\gamma}\begin{bmatrix} -\coth(\gamma a) & \dfrac{1}{\sinh(\gamma a)} \\[2mm] \dfrac{-1}{\sinh(\gamma a)} & \coth(\gamma a) \end{bmatrix}\begin{bmatrix} \hat{H}_y^b \\ 0 \end{bmatrix} \tag{6}
$$

In writing these expressions, the jump and boundary conditions have been inserted. These four equations determine the complex amplitudes $(\hat{B}_x^a, \hat{B}_x^b, \hat{B}_x^d, \hat{H}_y^b)$ in terms of the stator surface current density. Before proceeding, it is prudent to determine which amplitude is required.

Time-Average Force: With a pure traveling-wave excitation, the time-average force per unit y-z area is independent of y. This is true because, except for a temporal phase shift, each "slice" of the material, shown in Fig. 6.6.1, is stressed by the same fields. Formally, this force per unit area is found by integrating the stress tensor over the surfaces $S_1...S_4$ shown in the figure. The sum of these surfaces is like that of Fig. 4.2.1a, except that its extent in the y direction is arbitrary; it is the time-average rather than the space-average that is being taken. With the understanding that $z \to t$, the complex-amplitude averaging theorem, Eq. 2.15.14, is applicable. The time-average stress integrated
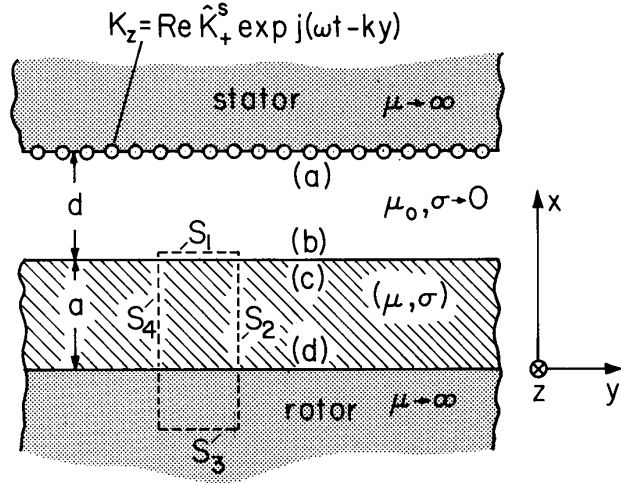
over surface S_2 cancels that integrated over surface S_4. The fields on S_3 are negligible,

$$\langle T_y \rangle_t = \frac{1}{2} \text{Re}[(\hat{B}_x^b e^{-jky})^* \hat{H}_y^b e^{-jky}] \tag{7}$$

and, as expected, the y dependence is eliminated. To eliminate the self-field term from this equation, Eq. 5b is substituted for $\hat{B}_x^b$:

$$\langle T_y \rangle_t = \frac{\mu_o}{2} \text{Re}\left[\frac{j(\hat{K}_+^s)^* \hat{H}_y^b}{\sinh(kd)}\right] \tag{8}$$

Thus, it is $\hat{H}_y^b$ that is required and so Eqs. 5b and 6a are equated and solved for $\hat{H}_y^b$:

$$\hat{H}_y^b = \frac{-\hat{K}_+^s}{\sinh(kd)\left[\frac{k}{\gamma}\frac{\mu}{\mu_o}\coth(\gamma a) + \coth(kd)\right]} \tag{9}$$

Substitution of this expression into Eq. 8 then gives the time-average force per unit area as a function of the stator surface current:

$$\langle T_y \rangle_t = -\frac{\mu_o}{2}\frac{|\hat{K}_+^s|^2}{\sinh^2(kd)} \text{Re}\frac{j}{\left[\frac{ka\mu}{\gamma a\mu_o}\coth(\gamma a) + \coth(kd)\right]} \; ; \; \gamma a \equiv \sqrt{(ka)^2 + jS_M} \tag{10}$$

where $S_M \equiv \mu\sigma a^2(\omega - kU)$. With a balanced two-phase excitation, $\hat{K}_+^s$ would be related to the terminal currents by 6.4.2 and 6.4.12.

The dependence of the time-average force on S_M, the normalized frequency as measured from the rotor frame of reference, is illustrated in Fig. 6.6.2. The function is odd in S_M. If the material velocity U exceeds the wave-phase-velocity ω/k, so that S_M is negative, the sign of the force is negative.

The dependence is somewhat similar to that for the thin-sheet interaction of Sec. 6.4 (see Fig. 5.13.2). A qualitative difference is that the deep-conductor force falls off less rapidly with increasing rotor-frame frequency than does the thin-sheet force. Two observations point to the origins of this difference. First, for S_M exceeding 2, the skin depth based on the rotor frame frequency, $\delta' \equiv \sqrt{2/|\omega-kU|\mu\sigma} = a\sqrt{2/|S_M|}$, is shorter than the conductor thickness. In the thick-conductor model, currents redistribute themselves in such a way that the effective L/R time constant remains on the order of the rotor-frame frequency (see discussion accompanying Eq. 6.2.10). Second, it is shown in Sec. 6.10 that whereas the thin-sheet model embodies a single natural temporal mode, the deep-conductor model retains an infinite number of such modes. At high frequencies, a spectrum of these contribute to the sinusoidal driven response, and tend to broaden the frequency dependence of the force.

Fig. 6.6.2. Time-average force/unit area acting on deep conductor in direction of traveling wave. ka=kd=1, $\mu=\mu_o$. The force is an odd function of $S_M \equiv \mu\sigma a^2(\omega - kU)$. The broken curve is the high-frequency asymptote given by Eq. 11.

The high-frequency limit of Eq. 10 is taken by recognizing that if $|S_M| \gg (ka)^2$, then $\gamma a \to (1 \pm j)\sqrt{|S_M|/2}$, where the upper and lower signs pertain for S_M positive and negative, respectively. As the magnitude of γa becomes large, $\coth(\gamma a) \to 1$.
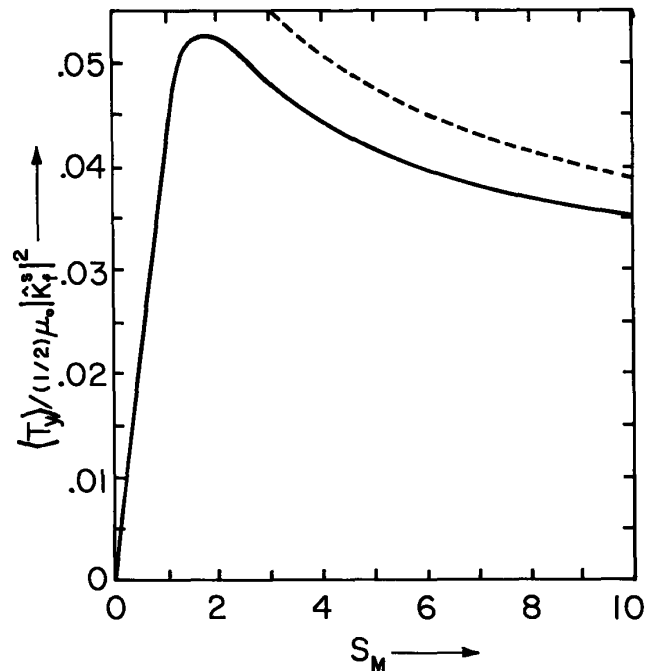
Thus, Eq. 10 becomes approximately

$$\langle T_y \rangle_t = \pm \frac{\mu_o}{2} \frac{|\hat{K}_+^s|^2}{\sinh^2(kd)} \frac{(ak)\frac{\mu}{\mu_o}\sqrt{|S_M|/2}}{[(ak)\frac{\mu}{\mu_o} + \sqrt{|S_M|/2}\coth(kd)]^2 + [\sqrt{|S_M|/2}\coth(kd)]^2} \tag{11}$$

This high frequency approximation is represented by the broken line curve of Fig. 6.6.2. Because of the skin effect, in this high-frequency limit, the force is inversely proportional to the square root of the rotor frequency. By contrast, in this limit with the thin-sheet model (represented by the first term in Eq. 6.4.11), the force varies inversely with the frequency.

Thin-Sheet Limit: What approximations are implicit to the thin-sheet model of Sec. 6.4? This is tantamount to asking what approximations are necessary if the thin sheet force for a pure traveling wave (the first term in Eq. 6.4.11) is to adequately approximate Eq. 10. It is clear from Eq. 10 that there are two measures of the conductor thickness a, one the quantity (ka) which is small compared to unity if $a < \lambda/2\pi$, where λ is the wavelength of the spatially periodic excitation. The other is γa (Eq. 10), which can alternatively be written in terms of a skin depth δ' based on the rotor frequency,

$$\gamma a = \sqrt{(ka)^2 + jS_M} = \sqrt{(ka)^2 \pm 2j(\frac{a}{\delta'})^2}; \quad \delta' \equiv \sqrt{\frac{2}{\mu\sigma|\omega - kU|}} = a/\sqrt{|S_M|/2} \tag{12}$$

In order for $|\gamma a| \ll |$, there are therefore two requirements, and these are the fundamental approximations validating the thin-sheet model:

$$ka \ll 1; \quad \frac{\delta'}{a} \gg 1 \tag{13}$$

With these approximations, $\coth \gamma a \to 1/\gamma a$ and Eq. 10 can be written in the form of the first term in Eq. 6.4.11. Note that $S_M = (ka)S_m$. In the limit (ka) $\ll$ 1, these expressions are in fact identical.

Conceptualization of Diffusing Fields: With the objective of picturing the space-time evolution of the fields in the conducting layer as a function of δ'/a and ka, remember that all fields have been represented in terms of

$$A = Re\hat{A}(x)e^{j(\omega t - ky)} = Re|\hat{A}(x)|e^{j[\omega t - ky + \theta(x)]} \tag{14}$$

where $\hat{A}(x)$ in general is given by Eq. 6.5.6, and in particular for the configuration considered in this section (where $H_y(0) = 0$ and hence $dA/dx(0) = 0$) is

$$\hat{A} = \hat{A}^c \frac{\cosh(\gamma x)}{\cosh(\gamma a)} \equiv |\hat{A}(x)|e^{j\theta(x)} \tag{15}$$

This expression can be deduced formally by manipulating the complex amplitudes, but is just as well found by inspection. From Eq. 15, the field intensity in the conductor follows from $\vec{H} = \nabla \times \vec{A}/\mu$ (Table 2.18.1), and the current density is

$$\hat{J} = \frac{1}{\mu} \nabla \times \nabla \times \vec{A} = -\frac{\nabla^2\vec{A}}{\mu} \Rightarrow \hat{J}_z = -\frac{1}{\mu}\left(\frac{d^2\hat{A}}{dx^2} - k^2\hat{A}\right) \tag{16}$$

or in particular, because $-j = \exp(-j\pi/2)$

$$\hat{J}_z = -\frac{\hat{A}^c}{\mu} j\mu\sigma(\omega - kU) \frac{\cosh(\gamma x)}{\cosh(\gamma a)} = -j\frac{S_M}{\mu a^2}\hat{A}(x) = \frac{S_M}{\mu a^2}|\hat{A}(x)|e^{j(\theta - \pi/2)} \tag{17}$$

Of course, $\hat{A}^c$ is determined from Eqs. 5 and 6 by the stator surface current density, but for the present purposes it is just as well to think of $\hat{A}^c$ as imposed at the air-gap surface of the conducting layer (at x = a). The amplitude and phase of $\hat{A}(x)$, defined by Eq. 15, are then typified by the distributions over the conductor cross section shown in Fig. 6.6.3. At any given plane x = constant in the conductor, the fields take the form of a sinusoid traveling in the y direction with the phase velocity ω/k. The amplitude of this wave, $|\hat{A}(x)|$, varies with distance into the conductor as shown in Fig. 6.6.3a. (Note that there is decay of the field in the $-x$ direction even if $\delta'/a \to \infty$. This is simply the decay characterizing Laplace's equation in free space. For the plots, ka = 1.) Points of the same phase on the traveling sinusoidal wave, say of phase θ_0, have the space-time relationship

$$ky = \omega t + \theta(x) - \theta_0 \tag{18}$$

That is, for values of y given by Eq. 18, the exponential in Eq. 14 becomes $\exp j\theta_0$, a complex constant. Thus, at any instant, the plot of $\theta(x)$ shown in Fig. 6.6.3b is equivalent to the (x-y) distribution of
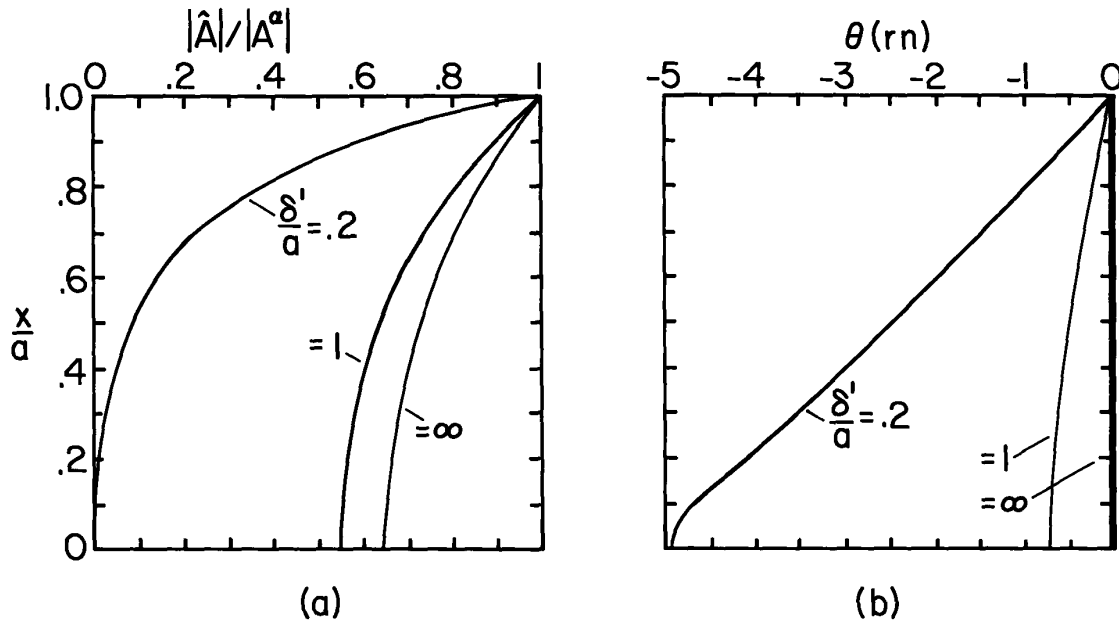
Fig. 6.6.3. Amplitude and phase of $A = \mathrm{Re}|\hat{A}(x)|\exp j(\omega t - ky + \theta(x))|$ for fields diffusing through conductors of Fig. 6.6.1. The parameter is the skin depth, based on the material frame frequency, normalized to the conductor thickness, δ'/a; $ka = 1$.

the points of a given phase on the sinusoidal traveling waves. For example, when $t = 0$, an $x - y$ plot of the zero crossing for a co-sinusoid is given by Eq. 18 with $\theta_0 = \pi/2$.

The distribution when $t = 0$ is now readily visualized in terms of the amplitude and phase plots of Fig. 6.6.3. As an example, Fig. 6.6.4 shows the distribution of A when $t = 0$ for $\delta'/a = 0.2$. As Eq. 18 shows, the time dependence is seen by simply letting this picture propagate to the right with the phase velocity ω/k.
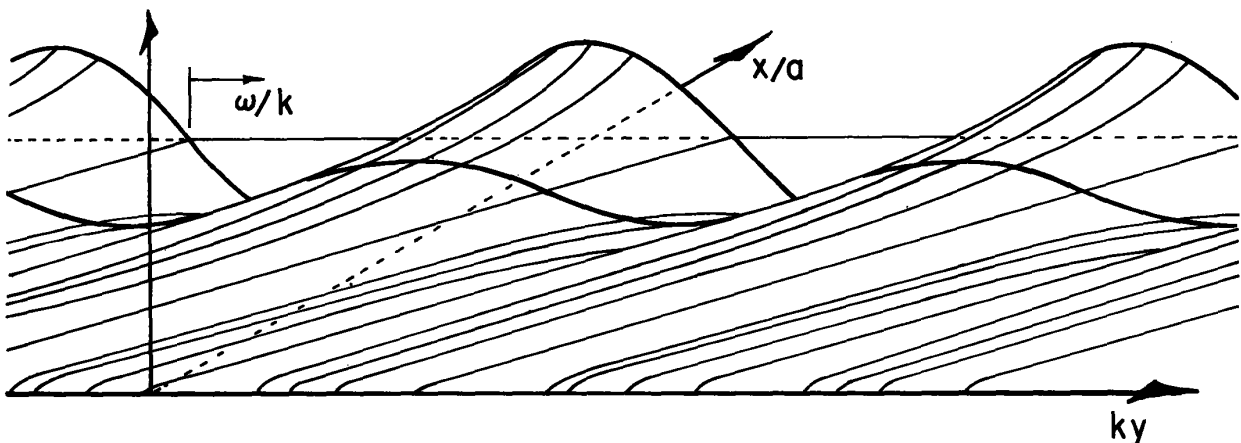

Fig. 6.6.4. Magnetic diffusion wave distribution A across conducting layer of Fig. 6.6.1 with pure traveling wave of excitation. For fields shown, phase velocity ω/k of wave exceeds material velocity U. As time proceeds, picture translates to the right with phase velocity ω/k.

The decay is of course least when the skin depth is largest, assuming a limiting value consistent with Laplace's equation. In this limit, the contours of constant phase in the x-y plane become parallel to the x-axis.

In the thin-sheet model, the Laplacian decay is negligible (ka << 1) and the skin depth is large enough compared to (a) that the amplitude and phase are essentially uniform over the cross section.

In the opposite extreme where the skin depth is short compared to the conductor thickness, there is little effect reflected back into the layer by the highly permeable backing material at x = 0. In this limit, the traveling wave leaves a trail of magnetic field in the conductor that appears at any given y plane as a rapidly attenuating wave with phases advancing in the -x direction.

For the picture shown, $S_M > 0$, meaning that the wave velocity exceeds that of the material. If the material moves faster than the wave, $S_M < 0$, and the sign of the imaginary part of γ is reversed. This reverses the sign of the phase shift. The lines of constant phase in a field picture like Fig. 6.6.4 now run to the right with increasing y rather than to the left. This is true even though the wave velocity ω/k is still to the right. To make this observation consistent with intuition, note that the material is moving even more rapidly to the right than the wave.

To emphasize the effect of the material motion, consider a thought experiment in which all parameters are fixed while the material velocity U is increased, starting at zero. At zero velocity, the picture is as in Fig. 6.6.4, with the skin depth determined by the imposed frequency ω alone. As the velocity is increased, the skin depth δ' increases. Hence, the decay and phase shift are reduced. At synchronism, the skin depth δ' is infinite, the decay is Laplacian and there is no phase shift. Further increase of the velocity results in a positive phase shift and a decreasing skin depth. The picture returns to that typified by Fig. 6.6.4, except that the constant phase lines "stream ahead" of the traveling wave.

The short skin depth approximation is the basis for a far-reaching boundary layer model, discussed in Sec. 6.8.

6.7 Electrical Dissipation

Induction interactions of the type exemplified in Sec. 6.6 involve electromechanical energy conversion at some price of electrical power converted to heat. In fact, one of the most common applications of induced currents is to the efficient electrodeless production of heat in the volume of a conducting material. But, even where the objective is electromechanical energy conversion, the heating is likely to be a significant consideration. In this section, general relations are derived that can be applied to any situation in which the canonical conducting layer of Sec. 6.5 is embedded.

Some preliminaries are required to have a way of representing power dissipated in terms of quantities evaluated at the surfaces of the layer. The magnetoquasistatic form of Poynting's theorem, Eq. 2.13.16 with terms given by Eq. 2.14.16, is written in the inertial (primed) frame moving with the material:

$$-\nabla' \cdot (\vec{E}' \times \vec{H}') - \frac{\partial}{\partial t'} (\frac{1}{2} \mu \vec{H}' \cdot \vec{H}') = \vec{E}' \cdot \vec{J}_f' \qquad (1)$$

Magnetization has been taken as linear, $\mu_0(\vec{H}' + \vec{M}') = \mu\vec{H}'$. For purposes of physical interpretation, note that the integral of this expression over a volume V' enclosing material of fixed identity takes the form of Eq. 2.13.12. This expression states that the total flux of power across the surface and into the volume either goes into increasing the total energy within the volume or it leaves the magnetoquasistatic subsystem in a way represented by the term on the right. In general, power can either leave as mechanical work done through the action of the magnetic force on the moving material, or it leaves as electrical dissipation. Because there is no velocity of the material in the frame for which Eq. 1 is written, the term on the right cannot include power flow into the mechanical subsystem. It must be the electrical dissipation density P_d.

For the present purposes, what is required is an integration of Eq. 1 over a volume that is fixed in the laboratory frame. Thus, Eq. 1 is rewritten in terms of fixed frame variables. That is, in accordance with Eq. 2.5.2, $\nabla' \to \nabla$ and $\partial( )/\partial t' \to \partial( )/\partial t + \vec{v} \cdot \nabla( )$. Also, because the system is magnetoquasistatic, $\vec{H}' = \vec{H}$ (Eq. 2.5.9b). Thus, Eq. 1 is equivalent to

$$P_d = - [\nabla \cdot (\vec{E}' \times \vec{H}) + \frac{\partial}{\partial t} (\frac{1}{2} \mu \vec{H} \cdot \vec{H}) + \vec{v} \cdot \nabla (\frac{1}{2} \mu \vec{H} \cdot \vec{H})] \qquad (2)$$

Because $\vec{v}$ is uniform, and hence $\nabla \cdot \vec{v} = 0$, the energy convection term can be taken inside the divergence:

$$P_d = -\nabla \cdot (\vec{E}' \times \vec{H} + \vec{v} \frac{1}{2} \mu \vec{H} \cdot \vec{H}) - \frac{\partial}{\partial t} (\frac{1}{2} \mu \vec{H} \cdot \vec{H}) \qquad (3)$$

In the sinusoidal steady state, the time rate of change makes no time-average contribution. This expression therefore makes it possible to evaluate the electrical power dissipated by evaluating fields on the enclosing surface. Consider again the planar layer of material described in Sec. 6.5. It is embedded in a system that is periodic in the y direction and is in the sinusoidal steady state. The volume over which the electrical dissipation is to be found has the fundamental length of periodicity in the y direction and has y-z surfaces denoted by α and β adjacent to the upper and lower surfaces of the layer (Fig. 6.7.1).
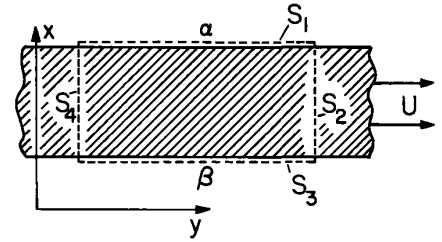
The fields are presumed to be generally represented in terms of a Fourier complex-amplitude series, in the form of Eq. 5.16.1. Integration of the time average of Eq. 3 over the volume is converted by Gauss' theorem to an integration of the quantity inside the divergence over the enclosing surface. Because of the periodicity, contributions to surfaces cutting through the layer, surfaces S_2 and S_4 and

Fig. 6.7.1. Control volume fixed in laboratory frame with fundamental periodicity length in y direction.

those in the x-y plane, cancel or are zero. It follows from the averaging theorem, Eq. 5.16.4, that the integration over the surfaces S_1 and S_2 is evaluated by multiplying the area A of S_1 or S_3 by the spatial average

$$\langle S_d \rangle_{yt} \equiv \frac{1}{A} \int_V \langle P_d \rangle_t \, dV = \frac{1}{2} \, \text{Re} \sum_{n=-\infty}^{+\infty} [(\hat{E}'_{zn} \hat{H}^*_{yn})^\alpha - (\hat{E}'_{zn} \hat{H}^*_{yn})^\beta] \tag{4}$$

Thus, the power dissipated over the cross section of the material within a volume having unit area in the y-z plane is evaluated in terms of complex amplitudes at the bounding surfaces. It is convenient to replace E'_z with variables already used in the transfer relations. By Ohm's law, Eq. 6.2.1 and Eq. 6.6.16,

$$\hat{E}'_z = \frac{\hat{J}_z}{\sigma} = -\frac{1}{\mu\sigma}\left(\frac{d^2\hat{A}}{dx^2} - k^2\hat{A}\right) \tag{5}$$

This expression is expressed in terms of the surface variables using Eq. 6.5.6 and the result evaluated at the respective surfaces. In view of the definition of γ^2, Eq. 6.5.5,

$$\begin{bmatrix} \hat{E}'^\alpha_z \\ \hat{E}'^\beta_z \end{bmatrix} = -j(\omega - kU)\begin{bmatrix} \hat{A}^\alpha \\ \hat{A}^\beta \end{bmatrix} \tag{6}$$

Thus, Eq. 4 can also be expressed as

$$\langle S_d \rangle_{yt} = -\, \text{Re} \sum_{n=-\infty}^{+\infty} j \, \frac{(\omega - k_n U)}{2} \, [\hat{A}^\alpha_n (\hat{H}^\alpha_{yn})^* - \hat{A}^\beta_n (\hat{H}^\beta_{yn})^*] \tag{7}$$

This is the required time- and space-average power dissipation per unit y-z area in the layer. Similar relations can be derived for the other configurations of Table 6.5.1. Application of Eq. 7 is made in Sec. 6.8.

6.8 Skin-Effect Fields, Relations, Stress and Dissipation

In the short skin-depth limit, the planar layer of Table 6.5.1 becomes representative of all of the configurations in that table. The skin depth δ' is identified by writing γ (defined with Eq. 6.5.5) as

$$\gamma = \sqrt{k^2 \pm j2/(\delta')^2}; \quad \frac{\omega}{k} \gtrless U; \quad \delta' \equiv \sqrt{\frac{2}{|\omega - kU|\mu\sigma}} \tag{1}$$

Note that the frequency that determines δ' is that experienced by the material; hence the appendage of a prime.

There are two approximations inherent to the model. First, the induced fields dominate over the "reactive" fields in determining the decay into the conductor:

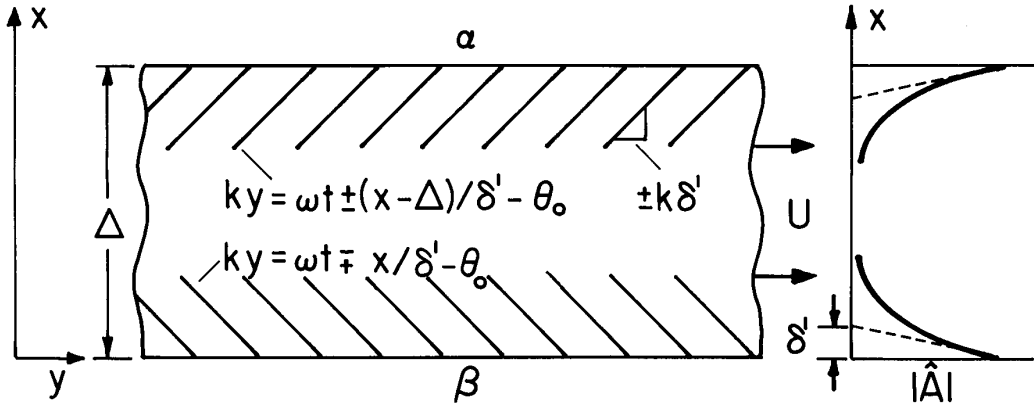$$k\delta' \ll 1 \Longrightarrow \gamma \to \frac{(1 \pm j)}{\delta'} \tag{2}$$

Fig. 6.8.1. Lines of constant phase move to right with velocity ω/k. For ω/k exceeding U, these lines form a "wake" to the left, as shown. If material velocity were to exceed ω/k, lines would slant to the right. Amplitude decays into material as shown, with depth for attenuation by e^{-1} equal to δ'.

Essentially, the skin depth is short compared to the wavelength of periodicity (divided by 2π).

Second, the skin depth is short compared to the thickness of the conductor:

$$|\gamma\Delta| \gg 1 \tag{3}$$

Then, the fields represented by the vector potential, Eq. 6.5.6, become two independent rapidly decaying waves confined to the respective surfaces:

$$A \simeq \mathrm{Re}\left[\hat{A}^\alpha e^{(x-\Delta)/\delta'}\; e^{j(\omega t - ky \pm \frac{(x-\Delta)}{\delta'})} + \hat{A}^\beta e^{-(x/\delta')}\; e^{j(\omega t - ky \pm \frac{x}{\delta'})}\right] \tag{4}$$

These fields are of course a limiting case of the example depicted by Figs. 6.6.3 and 6.6.4. In the short skin-depth limit, the lines of constant phase, sketched in Fig. 6.8.1, are exactly straight lines. It is assumed in the sketch that the wave phase velocity ω/k exceeds the material velocity U.

Transfer Relations: In the short skin-depth limit summarized by Eqs. 2 and 3, the planar layer transfer relations take a form representative of all of the configurations of Table 6.5.1. The mutual coefficients tend to zero as the thickness becomes large compared to δ', so that the short skin-depth transfer relations are

$$\begin{bmatrix} \hat{B}^\alpha_x \\ \\ \hat{B}^\beta_x \end{bmatrix} = -jk \begin{bmatrix} \hat{A}^\alpha \\ \\ \hat{A}^\beta \end{bmatrix} \simeq \frac{1}{2}(\mp 1 - j)k\mu\delta' \begin{bmatrix} -1 & 0 \\ \\ 0 & 1 \end{bmatrix} \begin{bmatrix} \hat{H}^\alpha_y \\ \\ \hat{H}^\beta_y \end{bmatrix} ; \left|\frac{\omega}{k}\right| \begin{matrix} > \\ < \end{matrix} U \tag{5}$$

According to these relations, in a frame of reference moving with the material, the fields diffuse into the conductor as though they were independent of y. That is, if the y component of the magnetic diffusion equation is written (Eq. 6.2.7), the contribution of the y derivative to the diffusion term is negligible compared to that from the x derivative. Thus, consistent with Eq. 5 is the approximation that

$$\frac{1}{\mu\sigma} \frac{\partial^2 H_y}{\partial x^2} = \left(\frac{\partial}{\partial t} + U\frac{\partial}{\partial y}\right)H_y \tag{6}$$

where the convective derivative on the right is the time rate of change for an observer moving with the material. If there were actually no y dependence, there would be no B_x. This is evident from the limit $k \to 0$ of Eq. 5. But, once having solved Eq. 6 to obtain H_y, the normal flux density can be found from the fact that $\hat{B}$ is solenoidal. The result would be Eq. 5. From a frame of reference moving with the conductor, short-skin-depth magnetic diffusion is as though the fields were independent of y.

Stress: But, without some y dependence there is no B_x and hence no magnetic stress. To compute the stress, the layer is enclosed by a control volume with surfaces as shown in Fig. 6.7.1. The force follows from an integration of the stress over this surface (as described in Sec. 4.2). The time-average force per unit y-z area tending to propel the slab in its direction of motion is found by

applying the time-average theorem, Eq. 5.16.4:

$$\left\langle T_y \right\rangle_{yt} = \left\langle B_x^\alpha H_y^\alpha - B_x^\beta H_y^\beta \right\rangle_{yt} = \frac{1}{2} \, \text{Re} \sum_{n=-\infty}^{+\infty} [\hat{B}_{xn}^\alpha (\hat{H}_{yn}^\alpha)^* - \hat{B}_{xn}^\beta (\hat{H}_{yn}^\beta)^*] \tag{7}$$

Evaluated using Eq. 5, this expression becomes

$$\left\langle T_y \right\rangle_{yt} = \pm \frac{1}{4} \sum_{n=-\infty}^{+\infty} \mu k \delta' (|\hat{H}_{yn}^\alpha|^2 + |\hat{H}_{yn}^\beta|^2) \tag{8}$$

For a given available magnetic pressure, μH_y^2, the shearing force is proportional to the skin depth and the wavenumber of the traveling wave.

The force in the x direction might be used to levitate a layer or system of layers. Suppose that the layer is surrounded by free space, where $\mu = \mu_o$. In general the space-time average is then written in terms of quantities that are continuous across the surface as

$$\left\langle T_x \right\rangle_{yt} = \left\langle \frac{\mu_o}{2} \left[\frac{1}{\mu^2} (B_x^\alpha)^2 - (H_y^\alpha)^2 \right] - \frac{\mu_o}{2} \left[\frac{1}{\mu^2} (B_x^\beta)^2 - (H_y^\beta)^2 \right] \right\rangle_{yt} \tag{9}$$

Because the x component of $\vec{H}$ is of order $(k\delta)$ smaller than the y component, this expression is consistently approximated by $B_x \approx 0$ and hence

$$\left\langle T_x \right\rangle_{yt} \simeq \frac{\mu_o}{4} \sum_{n=-\infty}^{+\infty} \left[-|\hat{H}_{yn}^\alpha|^2 + |\hat{H}_{yn}^\beta|^2 \right] \tag{10}$$

In the short skin-depth approximation, the normal force is simply the available magnetic pressure as it would exert itself on a layer of perfectly conducting material. In spite of the fact that the layer can be highly permeable, in the short skin-depth limit, the magnetic field "pushes" on the layer.

Dissipation: The power going into heating of the layer is computed in terms of the same surface variables as used to express the stress by applying Eq. 6.7.7. Evaluated using the short skin-depth transfer relations, Eqs. 5, it becomes

$$\left\langle S_d \right\rangle_{yt} = \frac{1}{2\sigma\delta'} (|\hat{H}_y^\alpha|^2 + |\hat{H}_y^\beta|^2) \tag{11}$$

For a given magnetic pressure, the power dissipation is inversely proportional to the skin depth. Hence, as the skin depth decreases, the heating increases and (from Eq. 8) the propulsion force decreases.

6.9 Magnetic Boundary Layers

An alternative title for Sec. 6.8 might be "magnetic boundary layers in the sinusoidal state." In essence, the skin-effect model is based on the same boundary layer approximation used in this section. Transverse magnetic diffusion dominates over that in the longitudinal (y) direction. Thus, in the magnetic diffusion equation, Eq. 6.2.7, the diffusion term is approximated by the second derivative with respect to the direction of field penetration, the x direction. With the conductor moving uniformly in the y direction, diffusion is therefore again governed by Eq. 6.8.3:

$$\frac{1}{\mu\sigma} \frac{\partial^2 H_y}{\partial x^2} = (\frac{\partial}{\partial t} + U \frac{\partial}{\partial y}) H_y \tag{1}$$

where it is presumed that $\partial( )/\partial z \approx 0$. Once the longitudinal field, H_y, is determined, the transverse field is determined by the rate-independent condition that the field be solenoidal:

$$\frac{\partial B_x}{\partial x} = -\mu \frac{\partial H_y}{\partial y} \tag{2}$$

The configuration of Fig. 6.9.1a is used in this section to illustrate the implications of the model. A relatively thick conductor moves to the right with velocity U. Just above the conductor, a fixed structure (perhaps windings driven by a current source) imposes a uniform current density $K_z = -H_o$ to the right of y = 0. This sheet is backed by an infinitely permeable material which extends over all

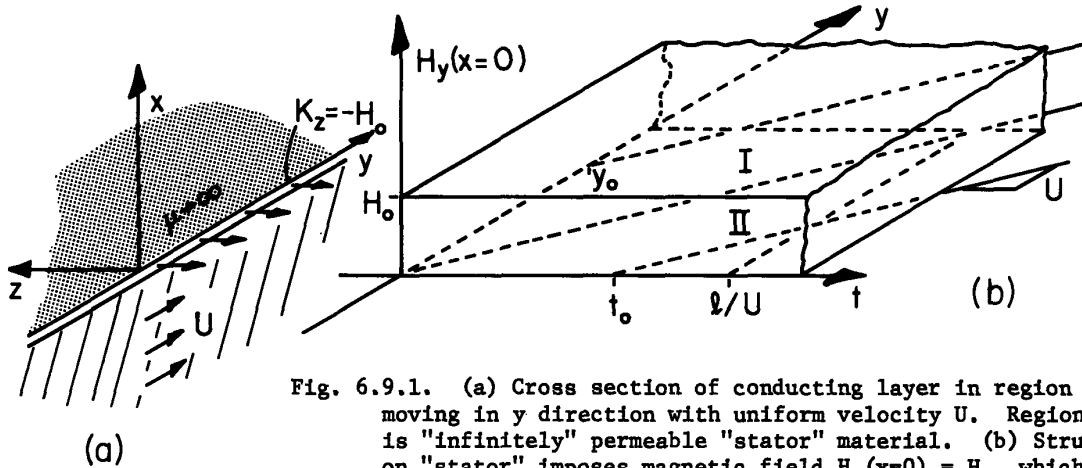Fig. 6.9.1. (a) Cross section of conducting layer in region x < 0
moving in y direction with uniform velocity U. Region x > 0
is "infinitely" permeable "stator" material. (b) Structure
on "stator" imposes magnetic field $H_y(x=0) = H_o$, which is
turned on over region y > 0 when t = 0.

of the region x > 0. Because the distance between sheet and conductor is small compared to other dimensions of interest, the boundary condition imposed on H_y at the conductor surface is that it be H_o to the right of y = 0 and that it vanish to the left. When t = 0, the current excitation is turned on. A summary of the space-time dependence imposed on H_y at the conductor surface is given in Fig. 6.9.1b. What are the implications of the boundary layer approximation for the evolution of H_y in the moving conductor? How can the boundary layer model be used to compute the drag and lift on the excitation structure?

One of the more dramatic of many practical and proposed applications involving a magnetic diffusion process having the nature of that considered here is shown in Fig. 6.9.2.[1] The structure is in that case a magnetically levitated train and the conducting material the "rail." The y coordinate measures distance relative to the vehicle. From this frame of reference, the turn-on transient settles into a steady state in which the current imaging that on the structure in a given conductor element penetrates into the conductor to a depth determined by the time elapsed since the element passed the leading edge of the structure.

The convective derivative on the right in Eq. 1, the time rate of change for an observer moving with the velocity U of the conductor, can be written in terms of time t' measured from the reference frame of a material element (see Secs. 2.4 and 2.5):

$$\frac{1}{\mu\sigma} \frac{\partial^2 H_y}{\partial x^2} = \frac{\partial H_y}{\partial t'} \tag{3}$$

with $\partial(\ )/\partial t'$ defined as the partial derivative holding $y' = y - Ut$ constant. The lines of constant y', shown in the y-t plane of Fig. 6.9.1b, have intercepts (y_o, t_o) respectively with the positive y and t axes. These parameters both denote the constant y' and distinguish between those lines in regions I and II of the y-t plane separated by the line y = Ut:

$$y = \begin{cases} Ut + y_o; & y > Ut, \text{ region I} \\ U(t - t_o); & y < Ut, \text{ region II} \end{cases} \tag{4}$$

From the material frame of reference, the magnetic diffusion represented by the boundary layer equation, Eq. 3, is one-dimensional. Only the time dependence of the boundary condition on H_y at x=0 reflects the temporal transient. For the particular excitation shown graphically by Fig. 6.9.1b, H_y is a step function that turns on when t = 0 so long as y > Ut. Physically, material elements having a distance from the leading edge greater than the transit time Ut, see a uniform magnetic field applied when t = 0. But, for y < Ut, an element experiences a step that turns on when t = t_o. This is the time when the element passes the leading edge of the structure at y = 0. These general remarks pertain regardless of the details of the field excitation, once it is turned on. For example, the excitation might be a traveling wave confined to y < 0 and turned on when t = 0.

Here, discusson is confined to an excitation that is constant for t > 0 and y > 0.
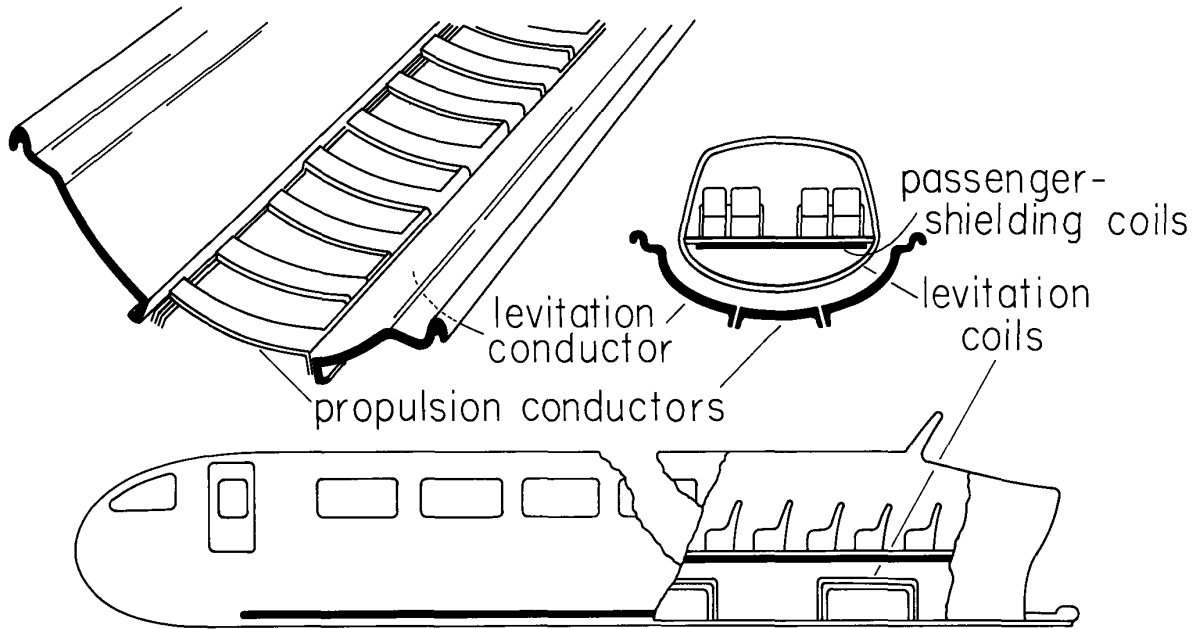
Fig. 6.9.2. Magneplane vehicle and "rail." Levitation results from interaction between conducting rail and magnetic fields from d-c excited superconducting coils mounted on vehicle. Currents are induced in rail by relative motion. The same d-c fields interact in synchronous fashion with traveling wave of magnetic field on center section of "rail" to provide propulsion.[1]

Similarity Solution: Can x and t' be related so that Eq. 3 becomes an ordinary differential equation? With t' understood to be the elapsed time since the field was turned on, it is expected that the field would have penetrated in the x-direction to a depth Δ_m typified by setting the magnetic diffusion time (defined with Eq. 6.2.9) equal to t' and solving for the length

$$\Delta_m = \sqrt{\frac{t'}{\mu\sigma}} \tag{5}$$

Thus, it is reasonable to scale the actual distance x to this length with a factor of 2 introduced to make the resulting equation assume a standard form

$$\xi \equiv \frac{x}{2}\sqrt{\frac{\mu\sigma}{t'}} \tag{6}$$

The conjecture is that the field intensity found at $x = x_1$ when the elapsed time from turn-on is $t' = t_1$ will be the same at time t where $x = x_1\sqrt{t/t_1}$. Evaluation of the derivatives in Eq. 3 justifies the supposition by converting the equation to

$$\frac{d^2H_y}{d\xi^2} + 2\xi\frac{dH_y}{d\xi} = 0 \tag{7}$$

In spite of the coefficient that depends on ξ, this equation has a simple solution satisfying the boundary condition $H_y(\xi = 0) = H_0$,

$$H_y = H_0[1 + \text{erf}(\xi)]; \quad \text{erf} \equiv \frac{2}{\sqrt{\pi}}\int_0^\xi e^{-\xi^2}d\xi \tag{8}$$

as can be seen by direct substitution. The error function,[2] erf(ξ), is normalized so that erf(ξ) → -1 as ξ → -∞.

In applying Eq. 8, it is necessary to distinguish between regions I and II of the y-t plane, Fig. 6.9.1b. In region I, the elapsed time since turn-on of the field is simply t'=t. Hence, Eq. 8

1. See H. H. Kolm and R. D. Thornton, "Electromagnetic Flight," Sci. American 229, 17-25 (1973).

2. Jahnke-Emde-Losch, Tables of Higher Functions, McGraw-Hill Book Company, New York, 1960, pp. 26-31.
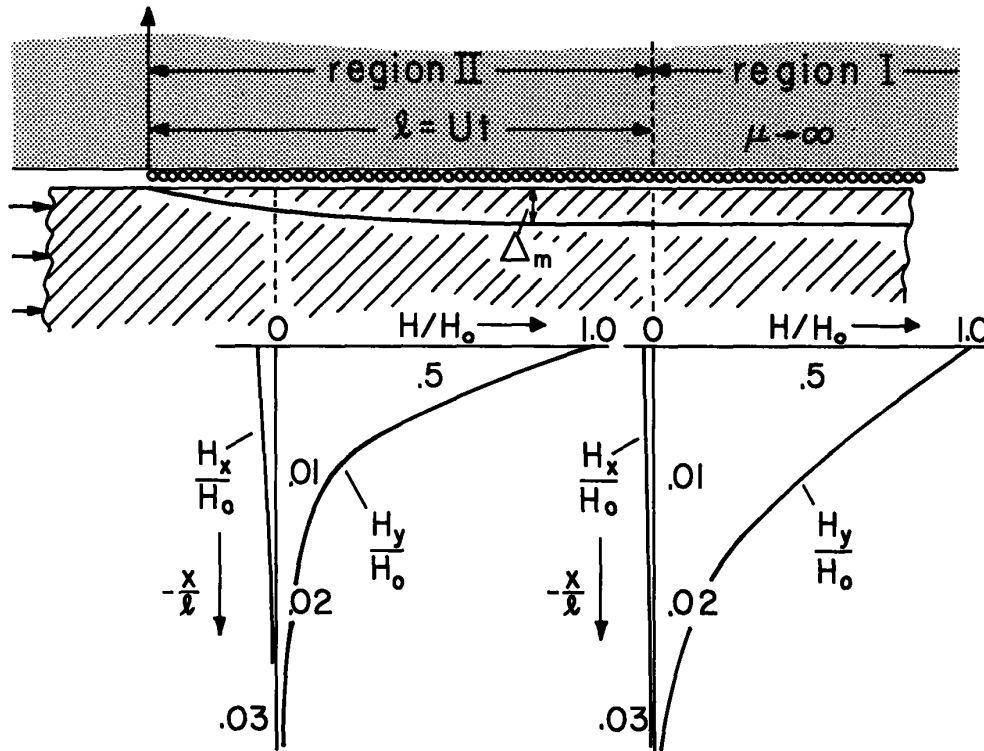
Fig. 6.9.3. Diffusion into moving conductor of magnetic field generated by current sheet $K_z = -H_o$
to right of $y = 0$ backed by highly permeable material and turned on when $t = 0$. Field
has stationary profile to left of $y = \ell = Ut$ and profile that is independent of y but in-
creasing its penetration with time to right of $y = Ut$. The plots show penetration of field
at $y = 0.25\ell$ and $y = \ell$ with $R_m \equiv \mu\sigma U\ell = 100$. Note that magnitude of H_x is much less than H_y.

with ξ defined by Eq. 6 with $t' \rightarrow t$ gives the x-t dependence of H_y. The plot of H_y for $y = \ell = Ut$ in
Fig. 6.9.3 illustrates the x-t dependence implied by the similarity solution. Region I is to the right
of this location, so to the right the field is independent of y and increasing its depth of penetration
with time.

In region II, between the leading edge and $y = Ut$, the elapsed time $t - t_o$ follows from Eq. 4b as
$t' = y/U$ and hence from Eq. 6

$$\xi = \frac{x}{2}\sqrt{\frac{\mu\sigma U}{y}}$$ (9)

With this parameter used in Eq. 8, it is clear that the field in region II is stationary, with the role
of t replaced by y/U. Thus, in region II, the boundary layer grows in thickness with increasing y but
remains constant in thickness at a given y. As time progresses, the front between the stationary field
of region II and the temporally evolving field of region I moves to the right so that finally the sta-
tionary condition prevails. Of course, at some distance ℓ, the depth of penetration may be large
enough to bring the finite thickness of the conductor into play. Alternatively, the length ℓ may reach
the length L of the structure used to impose the field. In this latter case, a second boundary layer
could be used to describe the field decay for $y > L$. The simple causal relation between excitation and
downstream response can be traced to there being no longitudinal diffusion included in the boundary-
layer model. There is no bow-wave in front of the leading edge and conditions downstream from the
region of interest have no influence.

Normal Flux Density: To find the drag force on the conducting layer, the distribution of B_x is
required. With H_y given by Eq. 8, it follows from Eq. 2 that

$$\frac{\partial B_x}{\partial x} = \begin{cases} 0 & ; y > Ut \\ \frac{\mu H_o}{2\sqrt{\pi y}}\sqrt{\frac{\mu\sigma U}{y}} \ xe^{-\frac{x^2}{4}\frac{\mu\sigma U}{y}} & ; 0 < y < Ut \end{cases}$$ (10)

.Holding y constant, this expression is integrated from $x = -\infty$ (where B_x must vanish) to x to obtain $\left(\int x e^{-ax^2} dx = \frac{1}{2} \int e^{-ax^2} dx^2 \right)$.

$$B_x = \begin{cases} 0 & ; \ y > Ut \\[2em] \dfrac{-\mu H_o e^{-\xi^2}}{\sqrt{\pi \mu \sigma U y}} & ; \ 0 < y < Ut \end{cases} \tag{11}$$

This distribution of B_x is also sketched in Fig. 6.9.3. Note that at the conductor surface, $B_x = \mu H_o / \sqrt{\pi R_m}$, where the magnetic Reynolds number $R_m = \mu \sigma U y$ is based on the distance from the leading edge. The boundary layer model is only valid if $\Delta_m \ll y$, and in Region II this is equivalent to $R_m \gg 1$. Thus, in the boundary layer approximation, B_x is much less than μH_o. As the boundary layer thickens in region II, the total magnetic flux in the y direction (which is proportional to $\mu H_o \Delta_m$) increases. Thus there must be a flux of B_x into the boundary layer from across the conductor surface and this is why a positive H_o implies a negative B_x.

Force: To find the total force on the conductor, the Maxwell stress is integrated over a surface enclosing the conductor and passing between the conductor and the structure in the x = 0 plane. The only contribution to the integration comes from this latter surface. Thus, the x-directed force on the conductor (the negative of the force tending to levitate the structure) due to a structure of length L and width w in the z direction is

$$f_x = w \int_o^L \frac{1}{2} \mu_o (H_x^2 - H_y^2)_{x=0} \, dy \tag{12}$$

In the boundary layer approximation, $H_x \ll H_y$. Therefore, consistent with this approximation is a normal force that is simply the product of the area of the conductor exposed to the magnetic stress and ($\frac{1}{2} \mu_o H_o^2$).

Because region I has $B_x \approx 0$ and hence no shear stress, the force in the direction of motion is simply

$$f_y = w \int_o^\ell [B_x H_y]_{x=0} \, dy = -2 \mu H_o^2 w \sqrt{\frac{\ell}{\pi \mu \sigma U}} \tag{13}$$

During the turn-on transient this drag force increases in proportion to $\ell = \sqrt{Ut}$ until ℓ reaches the full length L of the structure. Thereafter, the force is constant, given by Eq. 13 with $\ell = L$. With R_m again defined as $R_m = \mu \sigma UL$, this steady-state force can also be written as

$$f_y = -2\mu H_o^2 Lw / \sqrt{\pi R_m} \tag{14}$$

to make it clear that the final drag force is inversely proportional to the square root of the magnetic Reynolds number based on the length of the interaction region. From Eq. 14 it is clear that in the boundary layer limit, only a small fraction of the available magnetic stress, $\mu_o H_o^2$, contributes to the drag force.

6.10 Temporal Modes of Magnetic Diffusion

Temporal transients initiated from a state of spatial periodicity are introduced in Sec. 5.15. Just as that section revisited charge relaxation examples treated under sinusoidal steady-state conditions earlier in Chap. 5, this section returns to the configurations considered in Secs. 6.4 and 6.6. Analogies and contrasts between natural temporal modes of magnetic diffusion and charge relaxation are drawn by comparing the two magnetic configurations of this section to the corresponding electric pair from Sec. 5.15. It will be seen that there is a rather complete analogy between the thin sheet models. However, whereas a smoothly inhomogeneous conductor is required to give rise to an infinite set of natural modes in the charge relaxation bulk conduction model, here a uniform conductor is found to involve an infinite set of natural modes of magnetic diffusion.

Thin-Sheet Model: The natural frequencies for the system shown in Fig. 6.4.1 are given by setting the denominator of Eq. 6.4.6 equal to zero with $j\omega \rightarrow s_n$:

$$D(-js_n, k) = \sinh kd(-j + S_m \coth kd) = 0 \tag{1}$$

Only $S_{m+} \rightarrow S_m$ is considered in this expression because, in Eq. 1, k can be negative as well as positive. Solved for s_n, Eq. 1 becomes

$$s_n = +jkU - \left(\frac{k}{\mu_o \sigma_s}\right) \tanh(kd) \tag{2}$$

The thin-sheet model implies a single natural mode having a damping part determined by the effective "L/R" time constant $[\mu_o \sigma_s / k \tanh(kd)]$ and an oscillatory part caused by the relative motion of the conductor through the spatially periodic fields. Note the complete analogy between Eqs. 2 and 5.15.6. In the air gap, the single eigenmode, $A(x)$, associated with the eigenfrequency given by Eq. 2 is of the form of Eq. 2.19.3 with the coefficients adjusted to make the slope, dA/dx, zero at the stator surface ($H_y = 0$) and to make $\hat{A}$ continuous at the sheet surface. Because the normal flux density is continuous through the sheet, $\hat{A}(x)$ is essentially uniform over the sheet cross section. This is consistent with H_y (which is proportional to dA/dx) being zero on the surface of the highly permeable rotor next to the conducting sheet. The distribution of $A(x)$ is therefore given by
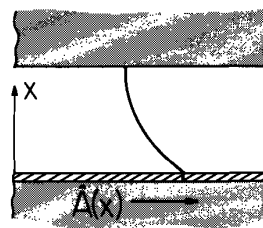

Fig. 6.10.1. Sheet model eigenmode.

$$\hat{A} = \begin{cases} \hat{A}^c \cosh k(x-d); & 0 < x < d \\ \hat{A}^c & ; \text{ inside sheet} \end{cases} \tag{3}$$

which is sketched in Fig. 6.10.1. The significance of the thin-sheet model is further appreciated by considering the higher order modes which it does not embody.

Modes in a Conductor of Finite Thickness: For the same conductor air-gap configuration, but with account taken of the conductor thickness, consider now the temporal modes implied by Eq. 6.6.9:

$$D(-js_n,k) = \sinh kd \left(\frac{k}{\gamma}\frac{\mu}{\mu_o} \coth \gamma a + \coth kd\right) = 0 \tag{4}$$

The frequency enters in this expression through the parameter γ_n, defined according to Eq. 6.5.5 by

$$\gamma_n = \sqrt{k^2 + j\mu\sigma(-js_n - kU)} \tag{5}$$

In general, solution of Eq. 4 involves finding the complex roots s_n that make the real and imaginary parts of $D(-js_n,k) = 0$. Because s_n enters only through γ_n, it is convenient to find the roots, γ_n, and then use Eq. 5 to find the implied roots s_n. Fortunately, an infinite number of roots, γ_n, are purely imaginary, as can be seen by recognizing that $\coth u = j\cot ju$ so that Eq. 4 becomes

$$\frac{\cot(j\gamma_n a)}{j\gamma_n a} = \frac{\mu_o}{\mu}\frac{\coth kd}{ka} \tag{6}$$

What is on the right in this expression is independent of $(j\gamma_n a)$ (and hence the frequency) and is real. Provided that $(j\gamma_n a)$ is real, what is on the left is also real. Hence, a graphical solution for the roots appears as shown in Fig. 6.10.2, where three of the roots $j\gamma_n a = \beta_n a$ (n = 0,1,2) are shown. Given the geometry and the layer permeability, which determine the right-hand side of Eq. 6, these roots are a set of numbers which can be inserted into Eq. 5 (solved for s_n) to determine the associated eigenfrequencies:

$$s_n = jkU - \frac{1}{\mu_o \sigma a^2}[(\beta_n a)^2 + (ka)^2] \tag{7}$$

Thus, there are an infinite number of modes, each having its own characteristic dependence on the transverse coordinate x. In terms of the vector potential $\hat{A}(x)$, Eq. 6.6.15 gives this dependence in the air gap, but this distribution is best found by simply adjusting the origin of the x coordinate so that a single hyperbolic function suffices to assure $dA/dx = 0$ at $x = a + d$ and $A = \hat{A}^c$ at $x = a$:

$$\hat{A}_n = \begin{cases} \hat{A}_n^c \dfrac{\cosh k[x - (a + d)]}{\cosh kd}; & a + d > x > a \\[2ex] \hat{A}_n^c \dfrac{\cosh \gamma_n x}{\cosh \gamma a} = \hat{A}_n^c \dfrac{\cos[\beta_n a(\frac{x}{a})]}{\cos \beta_n a}; & a > x > 0 \end{cases} \tag{8}$$

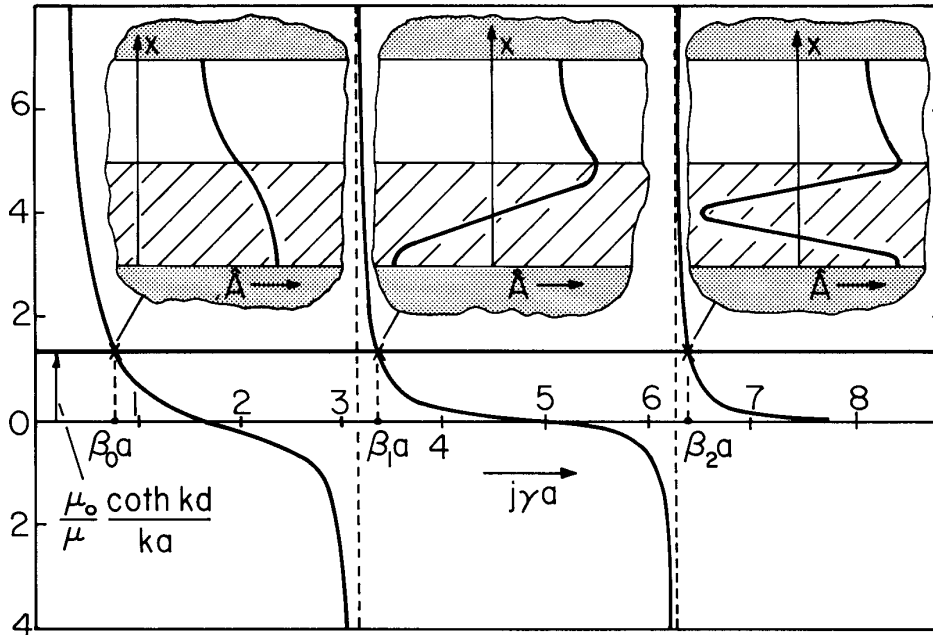The three eigenvalues found graphically in Fig. 6.10.2 are used to plot the eigenfunctions of Eq. 8 in

Fig. 6.10.2. Graphical solution for eigenvalues $(j\gamma_n a)$ satisfying Eq. 6. Inserts show associated eigenfunctions, $\hat{A}(x)$, with $ka = kd = 1$ and $\mu/\mu_o = 1$. Roots shown are $\beta_o a = 0.776$, $\beta_1 a = 3.364$ and $\beta_2 a = 6.401$.

the inserts to Fig. 6.10.2. Note that the $n = 0$ eigenmode approximates the sheet mode, Fig. 6.10.1.

Formally, the $n = 0$ mode becomes the thin-sheet mode in the limit of "small a." First, this means that $|\gamma a| \ll 1$, so that $\cot u \to 1/u$, and Eq. 6 can be solved approximately to obtain

$$(\gamma_o a)^2 = -\frac{\mu}{\mu_o} ka \tanh kd \tag{9}$$

Thus, the $n = 0$ eigenfrequency follows from Eq. 7 as

$$s_n \to jkU - \frac{ka}{\mu\sigma a^2} (\frac{\mu}{\mu_o} \tanh kd + ka) \tag{10}$$

If the second term in brackets can be dropped compared to the first, Eq. 10 indeed reduces to the eigenfrequency for the thin-sheet model, Eq. 2. Provided that $(\mu/\mu_o)\tanh kd$ is of the order of unity or more, this condition is met if $ka \ll 1$. This is the second condition to validate the thin-sheet model. Note that the two conditions for the thin-sheet model to approximate the lowest mode are just those given by Eq. 6.6.13.

An important proviso on the use of the thin-sheet model is apparent from these deductions. Unless the air gap is large compared to the sheet thickness, Eq. 10 does not follow from Eq. 9 and the thin-sheet model is not meaningful. In physical terms this is true because, in the model, magnetic energy storage within the sheet is ignored. To be meaningful, the sheet model must be incorporated into a system that allows for energy storage outside the sheet volume. In this example, that region is the air gap.

The general effect of decreasing the air gap can be seen from Fig. 6.10.2. As d is reduced, $\coth kd \to \infty$ and the horizontal curve moves upward. Thus, decreasing the gap decreases the values of $\beta_o \cdots \beta_\infty$ to the asymptotic roots $n\pi, n = 0,1,\cdots$. It follows from Eq. 7 that reducing d results in a decrease in the damping, in an increase in the time constant for decay of the sheet currents. This is reasonable, because the reduction in gap width results in an increased inductance for current loops in the y-z plane. Note that the $n = 0$ mode has an eigenvalue β_o that approaches zero as the gap is reduced. Hence, in Eq. 7, the term ka (which represents the energy storage within the sheet) must be retained. In the n=o mode, electrical dissipation is in the sheet while magnetic energy storage is largely in the gap. In the higher order modes, energy storage in the conducting layer is appreciable.

<u>Orthogonality of Modes</u>: Given an initial distribution of currents in the conducting layer, the eigenmodes can be used to represent the resulting transient. More generally, the modes play the role of the homogeneous solution in describing the response of a system to spatially periodic excitations, as described in Sec. 5.15. This homogeneous solution is the superposition of the eigenmodes

$$J_z = \sum_{n=-\infty}^{+\infty} \hat{J}_n(x) e^{-jky} e^{s_n t} \tag{11}$$

The process by which the amplitudes $J_n(x)$ are determined, given the initial conditions, is similar to that for a Fourier series. But, because the eigenmodes do not satisfy simple boundary conditions, it is not clear that these modes are orthogonal, in the sense that

$$\int_0^a \hat{J}_n \hat{J}_m dx = 0, \quad n \neq m \tag{12}$$

A proof that Eq. 12 is in fact valid follows from the differential properties of $\hat{J}_n$. The equation governing the current density modes follows from Eq. 6.6.16:

$$\hat{J}_z = -\frac{1}{\mu}\left(\frac{d^2}{dx^2} - k^2\right)\hat{A} \tag{13}$$

which is applied to Eq. 6.5.5 to see that

$$\frac{d^2\hat{J}_n}{dx^2} - \gamma_n^2 \hat{J}_n = 0 \tag{14}$$

Now, Eq. 14 is multiplied by another eigenmode, $\hat{J}_m$, and the result integrated over the cross section of the conducting layer. The first term can be integrated by parts to generate terms evaluated at the conductor surfaces and an integral that is symmetric in m and n:

$$J_m \frac{d\hat{J}_n}{dx}\bigg|_0^a - \int_0^a \left(\frac{d\hat{J}_m}{dx}\frac{d\hat{J}_n}{dx} + \gamma_n^2 \hat{J}_n \hat{J}_m\right) dx = 0 \tag{15}$$

These same steps can be carried out with the roles of m and n reversed, and if the resulting expression is subtracted from Eq. 15, an expression is obtained that begins to look like Eq. 13:

$$\left[\hat{J}_m \frac{d\hat{J}_n}{dx} - J_n \frac{d\hat{J}_m}{dx}\right]_0^a = (\gamma_n^2 - \gamma_m^2)\int_0^a \hat{J}_n \hat{J}_m dx \tag{16}$$

In the usual orthogonality condition (for example Eq. 4.5.28) homogeneous boundary conditions apply at the extremes of the interval. Here, the nature of the fields in the air gap must be considered to see that the left-hand side of Eq. 16 is zero. To express this in terms of A, observe from Eqs. 6.5.5 and 6.6.16 that

$$\hat{J}_z = -\frac{1}{\mu}(\gamma^2 - k^2)\hat{A} = -j\sigma(-js_n - kU)\hat{A} \tag{17}$$

$$\frac{d\hat{J}_z}{dx} = -j\sigma(-js_n - kU)\frac{d\hat{A}}{dx} \tag{18}$$

It follows from this last expression that because $\hat{H}_y = -(1/\mu)d\hat{A}/dx = 0$ at $x = 0$, the left-hand side of Eq. 16 evaluated at the lower limit is zero. Using Eqs. 17 and 18, what remains on the left can be written as

$$\left[\hat{J}_m \frac{d\hat{J}_n}{dx} - J_n \frac{d\hat{J}_m}{dx}\right]^a = \sigma^2(-js_n - kU)(-js_m - kU)\left[\hat{A}_m \frac{d\hat{A}_n}{dx} - \hat{A}_n \frac{d\hat{A}_m}{dx}\right]^a \tag{19}$$

That this quantity also vanishes follows from the properties of the gap fields. In the gap, where $\gamma^2 \to k^2$, Eq. 6.5.2 becomes

$$\frac{d^2\hat{A}_n}{dx^2} - k^2\hat{A}_n = 0 \tag{20}$$

Following steps analogous to those leading from Eq. 14 to Eq. 16, the field properties represented by this expression are exploited to show that

$$\left[A_m \frac{d\hat{A}_n}{dx} - \hat{A}_n \frac{d\hat{A}_m}{dx}\right]_a^{a+d} = 0 \tag{21}$$

Because $d\hat{A}/dx = 0$ at $x = a+d$ (the highly permeable stator surface), it follows that Eq. 19 vanishes. So long as $s_n \neq s_m$, Eq. 12 is valid.

6.11 Magnetization Hysteresis Coupling: Hysteresis Motors

Although induction devices of the type discussed in Secs. 6.4 and 6.6 are of the most common variety, they are particular examples from a class of machines in which sources are induced in the moving material. A somewhat less common member of the family is the hysteresis motor, known for its relatively constant torque over speeds ranging from "start" to synchronism.

It is the magnetization that is induced in the rotor of the hysteresis motor, rather than free current, as in the induction motor. Basic to the advantages of a hysteresis motor is the magnetization characteristic of the moving member. The currents in the induction machine depend on a time rate of change for their existence. They are rate-dependent, and so the magnitude and spatial phase of the currents in the moving member, and hence the ponderomotive force, depend on the relative velocity of material and traveling wave. By contrast, the spatial phase and magnitude of the magnetization induced in the moving material through a hysteresis interaction tends to be state-dependent.

The quasi-one-dimensional model pictured in Fig. 6.11.1a gives the opportunity to explore the physical basis for the hysteresis interaction in a quantitative way, but still avoid the extreme complexity inherent to the complete understanding of a practical device. The model harks back to ones developed in Secs. 4.12 and 4.13 for the variable capacitance machine. The stator surface current density, $K_z(y,t)$, is a wave traveling in the y direction. Windings backed by a highly permeable "stator" structure are perhaps as described in Sec. 6.4. Across the air gap, a, the moving material consists of a highly magnetized "core" covered by a layer of magnetic material having thickness b, and the magnetization characteristic shown in Fig. 6.11.1b.

As suggested by the permanent polarization interactions of Sec. 4.4, all that is required to obtain a net force in the y direction is a spatial phase lag between the induced magnetization and the magnetic axis of the current sheet. This phase delay is provided by the hysteresis, which insures that the driving current must provide a certain coercive magnetic field intensity before the magnetization can be reversed.
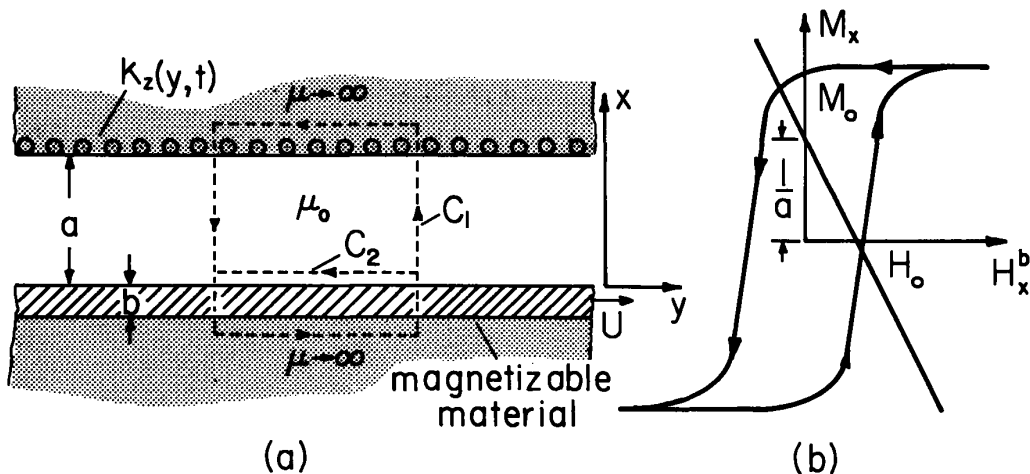

Fig. 6.11.1. (a) Cross-sectional view of quasi-one-dimensional model. (b) Magnetization characteristic approximated by hysteresis loop of Fig. 6.11.2.

At the risk of oversimplification, it is helpful to have a specific model in mind when dealing with the magnetization characteristic. Typically, magnetic materials used in electromechanical devices are polycrystalline, and can be thought of as composed of randomly oriented magnetlike domains. Application of a magnetic field intensity tends to align these domains, but because of what might be termed a "sticking friction," there is a threshold value of $\vec{H}$ at which the domains tend to flip into alignment with the imposed field. In some materials, complete orientation of the domains is very nearly achieved, once

this threshold has been exceeded. For that reason, and because it is then possible to make a relatively simple analytical model, the hysteresis loop is now approximated by the rectangular loop shown in Fig. 6.11.2. (To some degree, the characteristic depends on the rapidity with which the fields vary, but for present purposes the curve is shown, regardless of time rates of change.) The loop is double-valued, so the manner of arrival at a given point must be stipulated. That is, the magnetization induced by the applied field depends on the state of the fields, and not on their rate of change. But also, it depends in an essential way on the history of the magnetization.

Because of the highly permeable surfaces backing the current sheet and the magnetizable layer, the dominant magnetic field in the gap is x-directed. Ampère's law in integral form for the contour C_1 of Fig. 6.11.1 shows that

$$-K_z \Delta y = [H_x^a(y + \Delta y) - H_x^a(y)]a$$

$$+ [H_x^b(y + \Delta y) - H_x^b(y)]b \qquad (1)$$

In the limit $\Delta y \to 0$, this expression becomes

$$-K_z = a \frac{\partial H_x^a}{\partial y} + b \frac{\partial H_x^b}{\partial y} \qquad (2)$$

Fig. 6.11.2. Idealization of magnetization characteristic showing graphical solution $(a + b)/a = 2$.

The flux density in the x direction is continuous at the air-gap/magnetic-layer interface, so

$$H_x^a = H_x^b + M_x \qquad (3)$$

These last two expressions combine to relate the magnetization and field intensity in the magnetized layer,

$$-K_z = (a + b) \frac{\partial H_x^b}{\partial y} + a \frac{\partial M_x}{\partial y} \qquad (4)$$

For the present purposes, the surface current density is a given function of y, and so Eq. 4 can be integrated:

$$M_x = \frac{I}{a} - \frac{(a + b)}{a} H_x^b; \quad I \equiv -\int K_z dy \qquad (5)$$

Under the assumption that steady-state operation implies that neither M_x or H_x^b have space-average values, it follows that if $I(y,t)$ is defined as having no space-average value, the integration constant is zero. Because I is then a given function of y, Eq. 5 is a "load line" which can be used with the magnetization characteristic of Fig. 6.11.2 to graphically solve for (M_x, H_x). For illustrative purposes, the surface current is taken as a square wave, traveling to the right as sketched in Fig. 6.11.3a. Although there are no rate processes, it is essential to recognize that, if the moving member has a velocity less than that of the wave, the current distribution travels from left to right with respect to the material. The magnetic axis associated with the stator wave is indicated on Fig. 6.11.3a.

In the graphical solution of Eq. 5 and the magnetization characteristic depicted by Fig. 6.11.2, begin at point (a), where I/a has its peak amplitude. Because the wave travels from left to right, the magnetic material experiences a local evolution of I/a that proceeds from right to left on part (b) of Fig. 6.11.3. Thus, the points (a) - (f) denote the history of the (M_x, H_x) function in Fig. 6.11.2, and these points correspond to those indicated in Fig. 6.11.3. The graphical solutions for the magnetization and field intensity H_x are thus determined to be those shown in Fig. 6.11.3c. The induced magnetization lags the magnetic axis on the stator. The hysteresis has created the conditions for a force to the right.
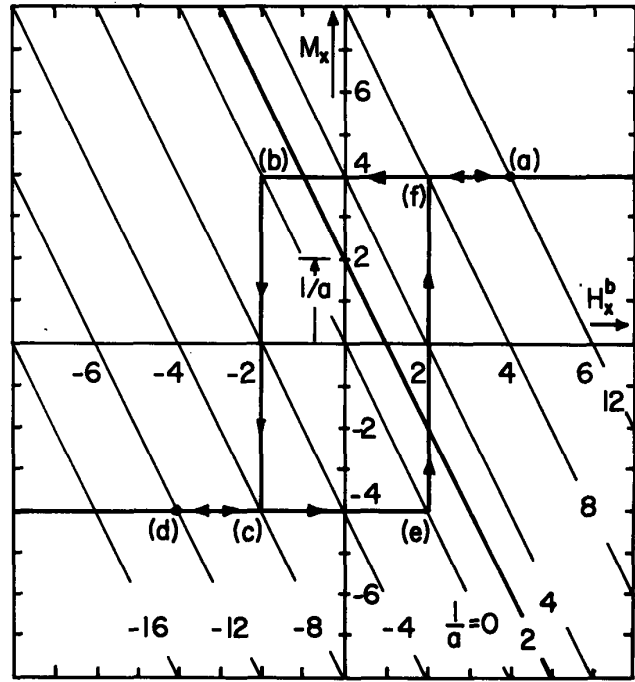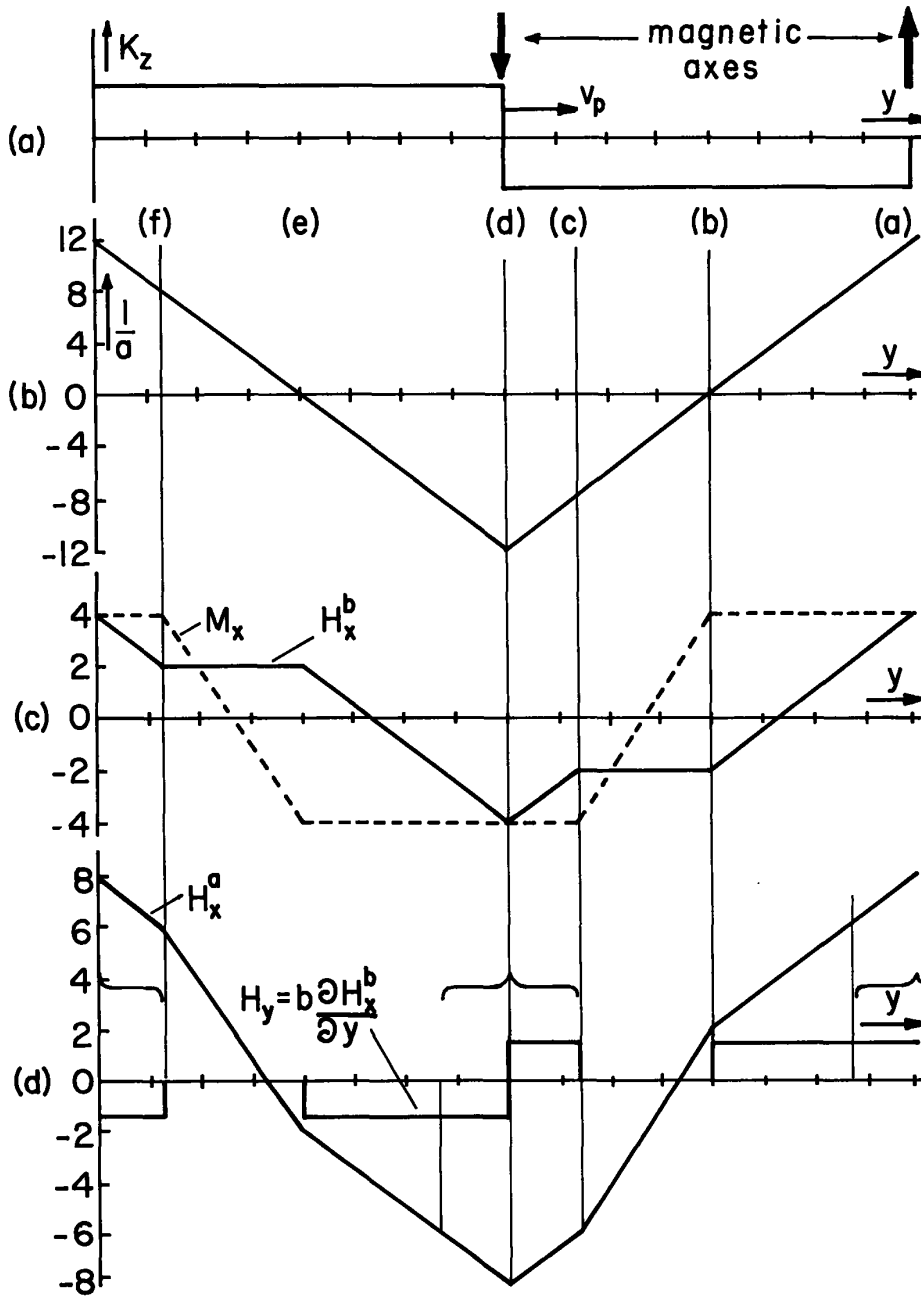
Fig. 6.4.3. (a) Distribution of surface current on "stator." (b) I/a; (c) distribution of magnetization and perpendicular magnetic field intensity in moving member; and (d) field components in adjacent air gap.

To determine the average force/unit area acting on one wavelength of the moving member, use is made of the free-space stress tensor. The force density is due entirely to magnetization, and might be taken as the Kelvin force density, Eq. 3.5.12 of Table 3.10.1, with $J_f = 0$. However, from Table 3.10.1, the stress tensor evaluated in free space is the same regardless of the model for the force density. This stress tensor is now integrated over a volume one wavelength long in the y direction, with its upper surface at $x = 0$ and its lower surface adjacent to the perfectly permeable substrate. Because there is no shear stress on the bottom surface, the average force/unit y-z area is

$$\left\langle T_y \right\rangle_y = \left\langle T_{yx} \right\rangle_y = \left\langle \mu_o H_x^a H_y^a \right\rangle_y = \left\langle \mu_o H_x^a H_y^b \right\rangle_y \tag{6}$$

Note that Eq. 6 cannot be completed unless the y component of the magnetic field intensity is known. Ampère's law in integral form, written for the contour C_2 of Fig. 6.11.1a, relates H_y to fields already determined,

$$-\Delta y H_y^b(x = 0) + b[H_x^b(y + \Delta y) - H_x^b(y)] = 0 \tag{7}$$

In the limit $\Delta y \to 0$,

$$H_y^b = b \frac{\partial H_x^b}{\partial y} \tag{8}$$

and so Eq. 6 can be written as

$$\left\langle T_y \right\rangle_y = b \mu_o H_x^a \frac{\partial H_x^b}{\partial y} \tag{9}$$

The components of $\vec{H}$ required to evaluate Eq. 9 are sketched in Fig. 6.11.3d with $\partial H_x^b/\partial y$ determined by taking the derivative of H_x^b from (c) of that figure, and H_x^a following from Eq. 3.

It is easy to take the spatial average indicated by Eq. 9, because the net contributions of those segments indicated in brackets in Fig. 6.11.3d will cancel, and the remaining segments clearly give a positive contribution. Thus, a space-average surface force density is deduced. It is independent of the material velocity U, so that the force-velocity curve is as shown in Fig. 6.11.4. Once the material velocity exceeds that of the wave, the relative direction of the current excitation is from right to left, and the arguments already outlined lead to an oppositely directed magnetic force.

The simple quasi-one-dimensional model illustrates why a hysteresis "torque-speed" characteristic gives a torque that tends to be independent of speed. The induced magnetization has an effect similar to that of permanent magnets, with the desired phase relationship between imposed magnetic axis and material magnetization determined by the history of the rotor as it is magnetized by the stator current.

For design purposes, a more complete representation of the rotor material would be desirable, although attempts to make use of analytical models in dealing with hysteresis motors are not numerous.[1]
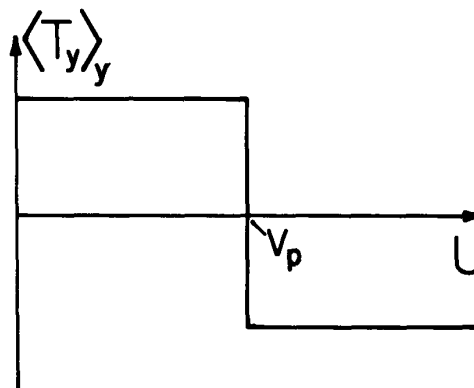
Fig. 6.11.4. Dependence of magnetic surface force density on speed for a hysteresis-type device.

1. M. A. Copeland and G. R. Slemon, "An Analysis of the Hysteresis Motor: I - Analysis of the Idealized Machine," IEEE Trans. on Power Apparatus and Systems, Vol. 82, April 1963, pp. 34-42, and II - "The Circumferential Flux Machine," ibid., Vol. 83, June 1964, pp. 619-625.